

# JGR Solid Earth

## RESEARCH ARTICLE

10.1029/2022JB024659

### Key Points:

- A new finite-element modeling tool was developed for global electromagnetic induction with general external sources and realistic Earth
- Accurate local ocean induction effects can be efficiently simulated by multi-resolution simulation grids
- Several Chinese coastal observatory data were analyzed for the first time, suggesting a dry mantle transition zone beneath southeast China

### Correspondence to:

Z. Ren,  
renzhengyong@csu.edu.cn

### Citation:

Yao, H., Ren, Z., Tang, J., & Zhang, K. (2022). A multi-resolution finite-element approach for global electromagnetic induction modeling with application to southeast China coastal geomagnetic observatory studies. *Journal of Geophysical Research: Solid Earth*, 127, e2022JB024659. <https://doi.org/10.1029/2022JB024659>

Received 25 APR 2022

Accepted 14 JUL 2022

## A Multi-Resolution Finite-Element Approach for Global Electromagnetic Induction Modeling With Application to Southeast China Coastal Geomagnetic Observatory Studies

Hongbo Yao<sup>1</sup> , Zhengyong Ren<sup>1,2</sup> , Jingtian Tang<sup>1,2</sup> , and Keke Zhang<sup>3</sup>

<sup>1</sup>Key Laboratory of Metallogenetic Prediction of Nonferrous Metals and Geological Environment Monitoring Ministry of Education, School of Geosciences and Info-Physics, Central South University, Changsha, China, <sup>2</sup>Hunan Key Laboratory of Nonferrous Resources and Geological Disaster Exploration, Changsha, China, <sup>3</sup>State Key Laboratory of Lunar and Planetary Sciences, Macau University of Science and Technology, Taipa, China

**Abstract** We present a multi-resolution finite-element approach for three-dimensional (3D) electromagnetic (EM) induction modeling in spherical Earth. First, the secondary electric field approach is employed so that both magnetospheric and ionospheric current sources are naturally considered. Second, the multi-resolution tetrahedral grids are used to approximate the heterogeneous crust and mantle, so that the local ocean effects at coastal and island observatories can be accurately simulated. Furthermore, a parallel goal-oriented hp-adaptive finite-element method with Nédélec vector elements is employed to guarantee the accuracy of solutions for arbitrary 3D conductivity distributions. Finally, two synthetic models are used to verify the accuracy and efficiency of our newly developed forward modeling solver. Results show that accurate solutions can be obtained for problems with several million to hundreds of millions of unknowns in a few minutes using 128 cores on a cluster. We apply this approach to correct the near-surface ocean effects for several unused Chinese coastal observatories by performing multi-resolution 3D modeling. The corrected data are inverted for the subsurface layered mantle conductivity structures. The conductivity model beneath southeast China is more resistive than that beneath northeast China by more than half an order of magnitude. By comparing the inverse models with the latest laboratory conductivity-depth profiles, the estimated transition zone water content is less than 0.01 wt% beneath southeast China irrespective of which laboratory data is used. Considering the low-velocity anomalies in this region, which suggest high-temperature structures, less water is expected. We, therefore, infer that the mantle transition zone beneath southeast China is dry.

**Plain Language Summary** Water in the mantle plays an important role in the dynamics and evolution of the Earth. Global scale electromagnetic induction studies can constrain the transition zone water content variations by imaging the electrical conductivity structures of Earth's mantle, which are highly sensitive to the amount and distribution of water. Geomagnetic data recorded by coastal observatories provide a valuable data source to study the conductivity and water content in the mantle. However, coastal geomagnetic data are considerably distorted by the ocean induction effects due to the large conductivity contrasts between oceans and continents. Therefore, we present a new finite-element modeling tool with multi-resolution tetrahedral grids to efficiently approximate the mantle and the heterogeneous crust regions, especially for ocean-continent interfaces so that the local ocean effects at coastal and island observatories can be accurately simulated. Using this new modeling tool to account for the local 3D ocean effects, we obtain a set of conductivity-depth profiles beneath southeast China using several unused geomagnetic observatory data. A comparison of our conductivity models with the latest laboratory measured conductivity data of mantle minerals and the seismic tomography imaging suggests the mantle transition zone beneath southeast China is dry.

## 1. Introduction

Understanding the composition, structure, and dynamics of Earth's mantle is one of the core tasks in Earth sciences. Although the seismic tomography technique can provide constraints on the physicochemical state and dynamics of the mantle by imaging its velocity structures (Fukao et al., 2009; Romanowicz, 2003), it can hardly distinguish the compositional and thermal effects. The global EM induction method (Kelbert et al., 2009; Kuvshinov, 2012), which employs long period geomagnetic variations measured by geomagnetic observatories or satellites, can give the electrical conductivity of Earth's mantle. As the electrical conductivity is sensitive to

temperature variations and the presence of melt and is strongly dependent on the amount and distribution of water (Karato, 2011; Yoshino, 2010), the global EM induction method has been widely used to study the thermochemical structure of Earth's mantle (Deschamps & Khan, 2016; Fukao et al., 2004; Kelbert et al., 2009; Khan & Shankland, 2012; Munch et al., 2018; Shimizu, Utada, et al., 2010; Utada et al., 2009). Currently, several global 3D mantle conductivity models have been proposed (Kelbert et al., 2009; Kuvshinov et al., 2021; Li et al., 2020; Semenov & Kuvshinov, 2012; Sun et al., 2015; Tarits & Mandéa, 2010; Velímský & Knopp, 2021). However, large discrepancies exist among these models. This is caused by multiple factors, such as the sparse and irregular distribution of geomagnetic observatories, the oversimplification of extraneous currents, improper consideration of surface ocean-continent conductivity contrasts, and the inaccuracy of forward modeling solvers, and the non-uniqueness of inversion. To reduce these discrepancies, this study concentrates on the improvement of accuracy of forward modeling solvers and accurate consideration of surface ocean effects.

Currently, there are a number of forward modeling solvers for global EM induction problems, which are based on the spherical harmonic and its hybrid variations (Hamano, 2002; Martinec, 1999; Tarits & Mandéa, 2010; Velímský & Martinec, 2005), the integral equation (IE) method (Koyama et al., 2014; Kuvshinov, 2008; Sun & Egbert, 2012), the finite difference (FD) method (Kelbert et al., 2008; Uyeshima & Schultz, 2000; Weiss, 2010, 2014; H. Zhang et al., 2019), and the finite element (FE) method (Everett & Schultz, 1996; Grayver et al., 2019; Ribaudo et al., 2012; Weiss & Everett, 1998; Yoshimura & Oshiman, 2002). The IE solvers with a contracting kernel (Koyama et al., 2014; Kuvshinov, 2008) have become the mainstream choices in nowadays global EM community (C. Chen et al., 2020; Fukao et al., 2004; Koch & Kuvshinov, 2015; Koyama et al., 2014; Kuvshinov et al., 2021 ; Munch et al., 2018; Semenov & Kuvshinov, 2012; Shimizu, Utada, et al., 2010; Utada et al., 2009) due to the advantages of only discretizing small anomalous domain and guaranteed convergence rate of iterative solvers. Therefore, unlike the other methods, the IE solvers demonstrated attractive performance in terms of both accuracy and efficiency (Kelbert et al., 2014). However, their advantages are counterbalanced by the nontrivial computations of dyadic Green's functions and the difficulty of dealing with large-scale arbitrary 3D conductivity distributions. Due to rapid development in parallel computational techniques, nowadays it is possible to greatly accelerate the computational speed of the FE solvers. In addition, the FE method can deal with arbitrary conductivity distributions and has a flexible grid adaptivity, which is crucial for approximating the realistic 3D Earth. Therefore, we use the FE method as the method of choice.

Two types of unstructured grids can be used to approximate the curved shell structure of the Earth, which are hexahedral grids (Grayver et al., 2019, 2021) and tetrahedral grids (Everett et al., 2003; Everett & Schultz, 1996; Ribaudo et al., 2012; Weiss & Everett, 1998; Yoshimura & Oshiman, 2002). Although hexahedral grids can obtain a good adaptivity for shell structures by using a high-order mapping function, tetrahedral grids can well approximate complex subsurface structures with a curved shape, even working in low-order mapping mode. Tetrahedral grids can also discretize both the spherical shell and the Earth's core, which is important when investigating the effects of metallic core on geomagnetic responses (Velímský & Finlay, 2011). Besides, different from hexahedral grids, refinement of tetrahedral grids can lead to conforming grids without hanging nodes. Therefore, we choose the tetrahedral grids to discretize the realistic 3D Earth.

At present, more and more geomagnetic data sets are available, proposing new requirements for developing the tetrahedral FE-based global EM forward modeling solvers. The first requirement is the capability of dealing with multiple external sources. The widely adopted magnetospheric ring current, which is dominating for geomagnetic variations from several days to several months, mainly provides resolution in and below the mantle transition zone (Kelbert et al., 2008; Semenov & Kuvshinov, 2012). To improve the resolution of upper mantle conductivity, the ionospheric Sq current, which is dominating at periods from several hours to 1 day, is needed (Egbert et al., 2021; Guzavina et al., 2019; Koch & Kuvshinov, 2015). These considerations motivate the development of FE-based global EM forward modeling solvers that can handle both magnetospheric ring current and ionospheric Sq current.

The second requirement is to accurately simulate the local ocean induction effects at coastal and island geomagnetic observatories. The ocean induction effects, which are due to the large conductivity contrast between oceans and continents, can significantly distort the geomagnetic responses for periods up to 20 days (Kuvshinov et al., 2002). Generally, the ocean induction effects are insufficiently simulated with global coarse grids (Everett et al., 2003; Kuvshinov et al., 2002; Utada et al., 2003; Weiss & Everett, 1998). To accurately account for the ocean effects, we need a mesh with very fine resolution nearby the observatories (C. Chen et al., 2020; Munch et al., 2018).

Using the global-to-regional technique, it is possible to efficiently simulate the ocean induction effects using the IE method (C. Chen et al., 2020; Kuvshinov et al., 2005) or the FD method (H. Zhang et al., 2019). But it is hardly feasible for previous FE-based modeling codes that utilize uniform tetrahedral grids (Everett & Schultz, 1996; Weiss & Everett, 1998; Yoshimura & Oshiman, 2002) due to the high computation consumption. Therefore, it is crucial to develop a new multi-resolution FE-based modeling code that can use fine grids regionally or locally around observatories and coarse resolution grids globally.

The third requirement is the capability of providing accurate EM responses for arbitrary 3D conductivity distributions. During inversion, the mantle conductivity structures are updated iteratively, a fixed forward mesh with the lowest order finite elements is not able to satisfy this requirement. To guarantee the accuracy of forward solutions, either the adaptive mesh refinement (h-refinement) or the high-order finite elements (p-refinement) are needed. Compared to the non-goal-oriented adaptive mesh refinement approach, which has been applied for global EM forward modeling on tetrahedral grids (Ribaudo et al., 2012), the goal-oriented adaptive mesh refinement approach (Oden & Prudhomme, 2001) is more robust since it can efficiently refine the subdomain of interest including the measurement profile (Ren et al., 2013). Compared to the lowest order finite elements, the high-order elements can offer a better trade-off between accuracy and computation time (Castillo-Reyes et al., 2019; Grayver & Kolev, 2015). With these ideas in mind, we anticipate that the combination of goal-oriented adaptive mesh refinement and high-order elements will provide an accurate and efficient tool for global EM modeling. However, a combination of goal-oriented adaptive mesh refinement and high-order elements is not yet applied for global EM induction modeling on tetrahedral grids.

The final requirement is computational efficiency. Due to the global nature of extraneous sources, modeling and inversion are performed on spherical Earth, and the memory and time cost can be extremely large. Previous studies with tetrahedral grids use conventional iterative solvers and preconditioners, such as the ILU iterative solver (Everett et al., 2003; Everett & Schultz, 1996; Weiss & Everett, 1998), the conjugate gradient method (Yoshimura & Oshiman, 2002), or the modified Newton-Raphson method (Ribaudo et al., 2012). Due to the lack of robust preconditioners, these iterative solvers need a large number of iterations and computation time to converge to accurate solutions or even diverge (Saad, 2003). In addition, existing FE codes using tetrahedral grids only work on serial (Everett & Schultz, 1996; Weiss & Everett, 1998; Yoshimura & Oshiman, 2002) or multi-thread computers (Ribaudo et al., 2012). To accelerate the computation, efficient iterative solvers with robust preconditioners and parallel computing techniques are required.

To meet the above requirements, we develop a new FE code for frequency domain global EM forward modeling using tetrahedral grids. By formulating the boundary value problem in terms of the secondary electric field, our code can handle complex magnetospheric and ionospheric sources in a unified manner. We also present a technique to generate multi-resolution tetrahedral grids utilizing several sophisticated computational geometry tools (Geuzaine & Remacle, 2009; Y. Zhang et al., 2018), enabling us to use fine resolution grids in the local area and coarse resolution in the far area and to efficiently simulate the local ocean effects. To guarantee the accuracy of solutions, we introduce a two-step hp-refinement strategy by combining the goal-oriented h-refinement method and the high-order Nédélec vector element (Nédélec, 1980). The goal-oriented h-refinement with the lowest order Nédélec vector element is first used to generate an optimal mesh distribution. A uniform p-refinement is then used to significantly increase the accuracy of numerical solutions on the final mesh. To accelerate the computation, we adopt a fully parallel implementation on massively parallel computing platforms.

The remaining sections of this manuscript are organized as follows. We first describe our new multi-source, multi-resolution finite-element approach in Section 2, followed by the validation of the forward modeling code in Section 3. In Section 4, we apply our approach to systematically investigate and correct the local ocean effects at several unused Chinese coastal geomagnetic observatories by performing multi-resolution modeling. Then we obtain a set of new conductivity profiles beneath China by inversion. We also discuss the physicochemical state beneath China by comparing our inverse conductivity models with the latest laboratory conductivity models and seismic imaging. Finally, we discuss and summarize our forward modeling approach and findings based on the interpretation of new Chinese coastal observatory data.

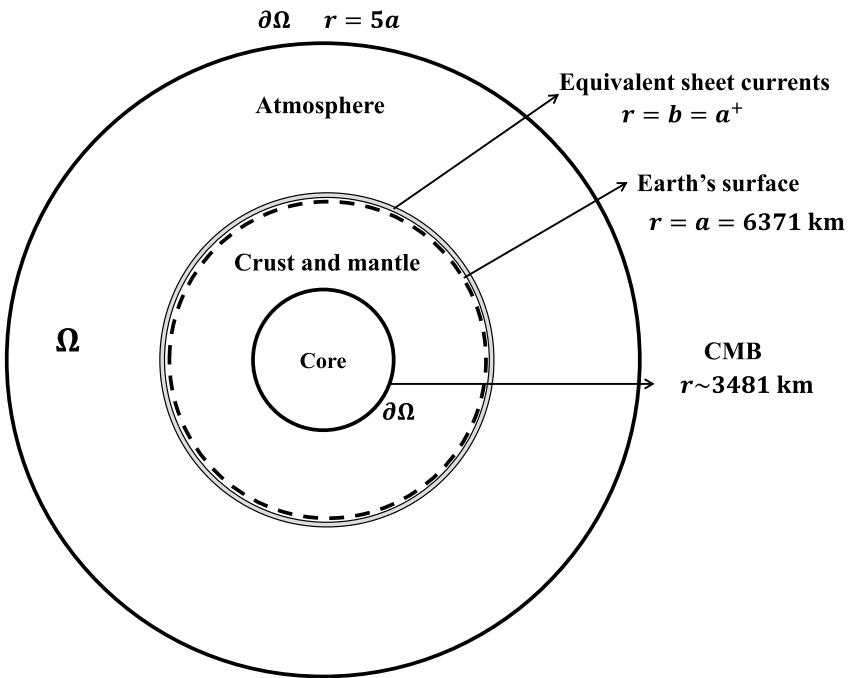


**Figure 1.** Illustration of the global-scale computational domain  $\Omega$ , which is composed of the atmosphere and the Earth's crust and mantle. The lower boundary is set to the core-mantle boundary (CMB), while the upper atmosphere boundary is set to five Earth's radii to decay the secondary (induced) field. The equivalent sheet current is assumed to flow just above Earth's surface with  $r = b = a^+$ .

## 2. Methods

### 2.1. Finite Element Discretization

Global EM induction problems require the solution of the EM responses in a spherical computational domain  $\Omega$  enclosed by a boundary  $\partial\Omega$  (Figure 1). Inside this bounded domain, the EM fields are governed by quasi-static Maxwell's equations which in the frequency domain (with a time-harmonic factor of  $e^{i\omega t}$ ) take the form.

$$\nabla \times \mathbf{E}(\mathbf{r}) = -i\omega\mu_0\mathbf{H}(\mathbf{r}), \quad (1)$$

$$\nabla \times \mathbf{H}(\mathbf{r}) = \sigma(\mathbf{r})\mathbf{E}(\mathbf{r}) + \mathbf{J}^{\text{ext}}(\mathbf{r}), \quad (2)$$

where  $\mathbf{E}(\mathbf{r})$  and  $\mathbf{H}(\mathbf{r})$  are the electric and magnetic fields, respectively,  $\mathbf{r} = (r, \theta, \phi)$  with  $r$ ,  $\theta$  and  $\phi$  are respectively the radial distance from Earth's center, colatitude, and longitude,  $i = \sqrt{-1}$  is the imaginary unit,  $\omega$  is the angular frequency,  $\mu_0$  is the magnetic permeability of free space,  $\sigma(\mathbf{r})$  is the electrical conductivity,  $\mathbf{J}^{\text{ext}}(\mathbf{r})$  denotes the extraneous electric current which will be discussed later. The dependence of EM fields and electric current on  $\omega$  is omitted but implied.

We first derive the boundary value problem. The 3D electrical conductivity structure of the Earth  $\sigma(\mathbf{r})$  can be decomposed into a 1D reference structure  $\sigma_0(r)$  and a conductivity perturbation  $\delta\sigma(\mathbf{r})$ , that is  $\sigma(\mathbf{r}) = \sigma_0(r) + \delta\sigma(\mathbf{r})$ . The perturbation includes the surface distribution of oceans and continents and the mantle heterogeneities. The extraneous current  $\mathbf{J}^{\text{ext}}(\mathbf{r})$  generates the primary electric  $\mathbf{E}_0$  and magnetic  $\mathbf{H}_0$  fields in the 1D reference model  $\sigma_0(r)$  with governing Maxwell's equations.

$$\nabla \times \mathbf{E}_0(\mathbf{r}) = -i\omega\mu_0\mathbf{H}_0(\mathbf{r}), \quad (3)$$

$$\nabla \times \mathbf{H}_0(\mathbf{r}) = \sigma_0(r)\mathbf{E}_0(\mathbf{r}) + \mathbf{J}^{\text{ext}}(\mathbf{r}). \quad (4)$$

Then the induced current  $\delta\sigma(\mathbf{r})\mathbf{E}_0(\mathbf{r})$  in the conductivity perturbation generates the secondary electric field  $\mathbf{E}_s = \mathbf{E} - \mathbf{E}_0$  and the secondary magnetic field  $\mathbf{H}_s = \mathbf{H} - \mathbf{H}_0$ . The corresponding governing equations as shown below are derived by subtracting Equations 3 and 4 from Equations 1–2

$$\nabla \times \mathbf{E}_s(\mathbf{r}) = -i\omega\mu_0\mathbf{H}_s(\mathbf{r}), \quad (5)$$

$$\nabla \times \mathbf{H}_s(\mathbf{r}) = \sigma(\mathbf{r})\mathbf{E}_s(\mathbf{r}) + \delta\sigma(\mathbf{r})\mathbf{E}_0(\mathbf{r}). \quad (6)$$

Taking the curl of Equation 5 and using Equation 6 to eliminate the secondary magnetic field  $\mathbf{H}_s$ , we obtain the secondary field formulation for the electric field

$$\nabla \times \nabla \times \mathbf{E}_s + i\omega\mu_0\sigma\mathbf{E}_s = -i\omega\mu_0\delta\sigma\mathbf{E}_0 \quad \text{in } \Omega, \quad (7)$$

where the computational domain  $\Omega$  is composed of the atmosphere and the Earth's crust and mantle (Figure 1). Hereinafter, the dependence of conductivity and EM fields on  $\mathbf{r}$  is omitted but implied. Assuming that the variations of the secondary field decay approximately to zero at the upper atmosphere boundary and lower core-mantle boundary, the Neumann boundary condition can be imposed at these boundaries

$$\mathbf{e}_r \times \nabla \times \mathbf{E}_s = 0 \quad \text{at } \partial\Omega. \quad (8)$$

Please note that we do not enforce the boundary condition at the core-mantle boundary if the core is included in the model.

We now discuss the extraneous electric currents  $\mathbf{J}^{\text{ext}}(\mathbf{r})$ . For the extraneous magnetospheric and ionospheric currents considered here, it is more convenient to work with the *equivalent sheet currents* (Schmucker, 1985). From a physical point of view, these equivalent currents can reproduce exactly the external or the internal part of an observed geomagnetic field (Schmucker, 1985). Assuming these equivalent currents are flowing within a thin spherical sheet outside Earth, and due to the linearity of Maxwell's equations with respect to the extraneous source, these equivalent sheet currents can be expressed with the linear combination of external source coefficients  $\epsilon_n^m$  and unit sources  $\mathbf{J}_n^{m,\text{unit}}$

$$\mathbf{J}^{\text{ext}}(\mathbf{r}) = \sum_{n,m} \epsilon_n^m(\omega) \mathbf{J}_n^{m,\text{unit}}(\mathbf{r}). \quad (9)$$

Using the spherical harmonic representation of the magnetospheric and ionospheric current systems, the unit source has the form (Kuvshinov & Semenov, 2012)

$$\mathbf{J}_n^{m,\text{unit}}(\mathbf{r}) = \frac{\delta(r-b)}{\mu_0} \frac{2n+1}{n+1} \left(\frac{b}{a}\right)^{n-1} \mathbf{e}_r \times \nabla_{\perp} Y_n^m(\theta, \phi), \quad (10)$$

where  $\delta(r-b)$  is the Dirac Delta function,  $a = 6,371$  km is the Earth's mean radius,  $b = a^+$  denotes the location of the equivalent sheet current, which is assumed to flow just above Earth's surface,  $\mathbf{e}_r$  is the radial unit vector,  $\nabla_{\perp}$  is the angular part of gradient operator  $\nabla = \mathbf{e}_r \frac{\partial}{\partial r} + \frac{1}{r} \nabla_{\perp}$ ,  $Y_n^m(\theta, \phi) = P_n^{|m|}(\cos \theta) e^{im\phi}$  are the spherical harmonic functions with  $P_n^{|m|}(\cos \theta)$  being the Schmidt quasi-normalized associated Legendre functions of degree  $n$  and order  $|m|$ .

For the magnetospheric currents, the double sum in Equation 9 has the form (Kuvshinov & Semenov, 2012)

$$\sum_{n,m} = \sum_{n=1}^{N_{\text{ext}}} \sum_{m=-n}^n, \quad (11)$$

where  $N_{\text{ext}}$  is the maximum cut-off degrees for the external coefficients. For the periodic ionospheric Sq variations, we consider the first six harmonics with angular frequencies of  $\omega_k = \frac{2\pi k}{T}$ , where  $k = 1, 2, \dots, 6$  and  $T = 24$  hr is the fundamental period of Sq variations. The harmonics with  $k > 6$  are ignored due to their insignificant contributions (Guzavina et al., 2019). Using the spherical harmonic representation of Schmucker (1999), the double sum in Equation 9 for the frequency  $\omega_k$  is given by

$$\sum_{n,m} = \sum_{m=k-1}^{k+1} \sum_{n=m}^{m+3}. \quad (12)$$

We finally describe the finite element discretization briefly. The primary electric field  $\mathbf{E}_0$  in Equation 7 is computed analytically by solving Equations 3 and 4, using the recursive formulation of Kuvshinov and Semenov (2012) for

a 1D reference conductivity model. For arbitrary 3D conductivity perturbations, which cause the secondary EM fields, we solve the curl-curl electric field Equation 7 using the tetrahedral finite-element method. The computational domain  $\Omega$  is discretized into a set of tetrahedral elements, the secondary electric field  $\mathbf{E}_s$  is discretized as

$$\mathbf{E}_s = \sum_{j=1}^{N_u} \mathbf{N}_j E_{sj}, \quad (13)$$

where  $N_u$  is the total number of unknowns,  $\mathbf{N}_j$  is the  $j$ th Nédélec vector basis function (Nédélec, 1980), and  $E_{sj}$  is the  $j$ th unknown secondary electric field associated with edges, faces, and volume of the tetrahedral elements. The Galerkin weighted residual method (Jin, 2014) is adopted to generate the system of linear equations

$$\mathbf{K}\mathbf{U} = \mathbf{F}, \quad (14)$$

where  $\mathbf{U}$  is a vector of the unknown secondary electric field,  $\mathbf{K}$  and  $\mathbf{F}$  are:

$$K_{ij} = \iiint_{\Omega} (\nabla \times \mathbf{N}_i) \cdot (\nabla \times \mathbf{N}_j) + i\omega\mu_0\sigma \mathbf{N}_i \cdot \mathbf{N}_j \, dv, \quad (15)$$

$$F_i = - \iiint_{\Omega} i\omega\mu_0\delta\sigma \mathbf{N}_i \cdot \mathbf{E}_0 \, dv. \quad (16)$$

After obtaining the secondary electric field, the total electric  $\mathbf{E}$  and magnetic  $\mathbf{H}$  fields can be obtained by  $\mathbf{E} = \mathbf{E}_0 + \mathbf{E}_s$ ,  $\mathbf{H} = \mathbf{H}_0 - 1/(i\omega\mu_0)\nabla \times \mathbf{E}_s$ .

## 2.2. Accuracy Enhancement

Several strategies are proposed to improve the accuracy of solutions. First, we present a multi-resolution tetrahedral grid approach to generate high quality initial meshes (Section 2.2.1). Second, we combine the goal-oriented h-refinement (Oden & Prudhomme, 2001) and high-order tetrahedral Nédélec elements (Nédélec, 1980) and propose a two-step hp-adaptive refinement scheme. In the first step, we design a goal-oriented error estimator for the secondary electric field formulation to drive the adaptive h-refinement (Section 2.2.2). Then an optimal mesh distribution can be obtained. In the second step, we utilize uniform p-refinement on the final mesh to further improve the accuracy of solutions (Section 2.2.3). Compared to the adaptive high-order method of Grayver and Kolev (2015), in which high-order hexahedral elements are used for each adaptive mesh refinement iteration, our scheme may be more computationally efficient since the computationally demanding high-order elements are only used for the final mesh.

### 2.2.1. Generation of Initial Multi-Resolution Tetrahedral Grids

The tetrahedral grids used by previous FE-based global EM forward modeling solvers are uniform resolution, which has the points distributed uniformly over the Earth's surface (Everett & Schultz, 1996; Yoshimura & Oshiman, 2002). A more efficient strategy is to use multi-resolution grids, which support fine resolution grids in regional/local areas and coarse resolution in the far area.

This study presents a workflow for generating multi-resolution tetrahedral grids in spherical geometry based on recently developed computer tools. Specifically, we exploit the spherical triangular tessellation (STT) tool (Y. Zhang et al., 2018) for variable-resolution surface triangular mesh generation and Gmsh (Geuzaine & Remacle, 2009) for tetrahedral mesh generation of Earth's interior. To divide the spherical surface into triangular meshes, STT starts with an icosahedron, then recursively subdivides facets of the icosahedron and maps the vertices onto the spherical surface. To allow for variable resolutions, STT implemented several constraint conditions which can locally refine the surface mesh at control points, along control lines, or within control polygons. STT uses subdivision level  $n$  to control mesh resolution, the angular resolution for subdivision level  $n$  is about  $60^\circ/2^n$ . For a 6-th level STT surface mesh, the resolution is about  $1^\circ$ . Gmsh is a 3D finite element mesh generator, it supports flexible and high-quality tetrahedral mesh generation using the Delaunay algorithm.

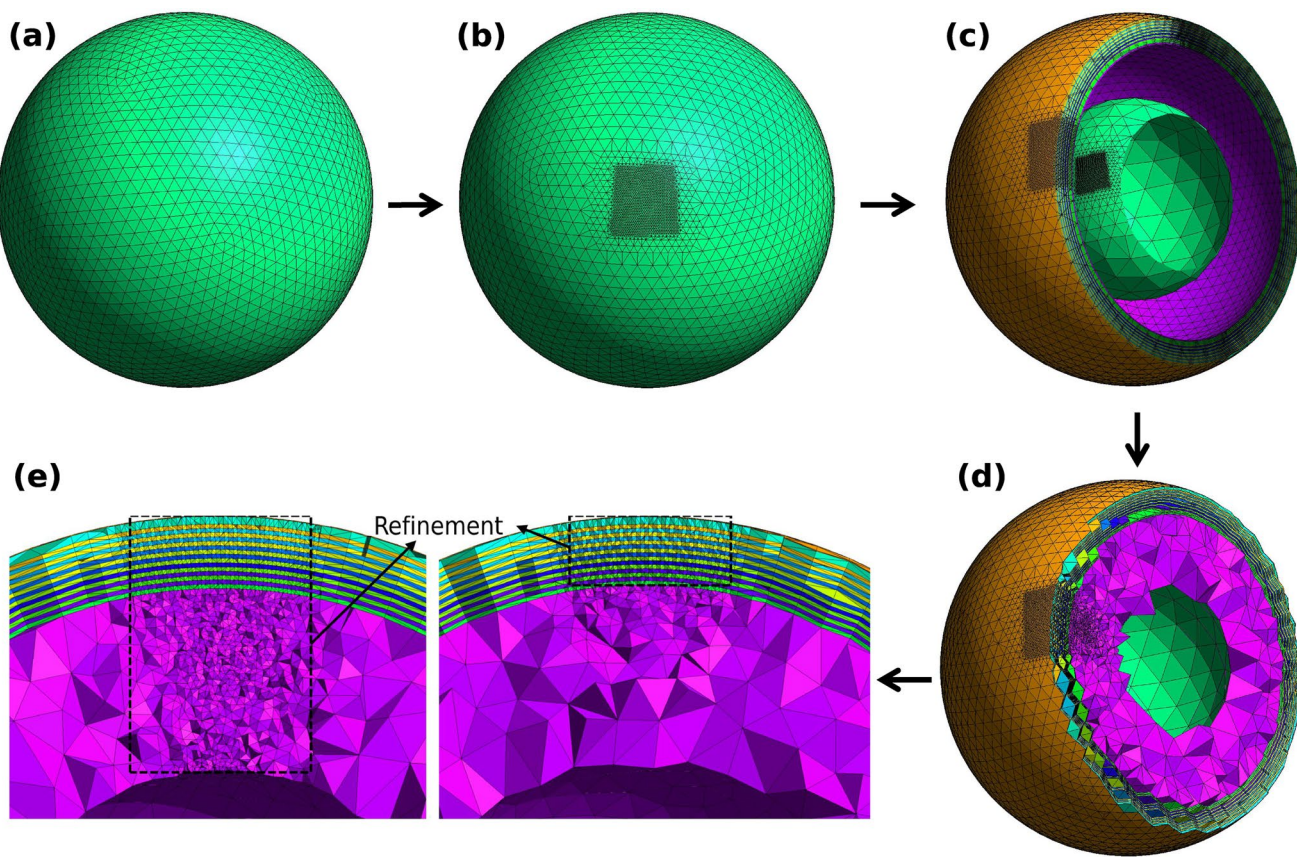


**Figure 2.** Illustration of the workflow for generating multi-resolution tetrahedral grids for spherical Earth. (a) A surface mesh with uniform spherical triangular tessellation. (b) A surface mesh with two-level multi-resolution spherical triangular tessellation, a high-resolution region is near geomagnetic observatory. (c) Multi-resolution spherical triangular tessellation for layered spherical Earth. (d) Multi-resolution tetrahedral grids for spherical Earth with higher resolution regionally near observatories and lower resolution globally. (e) Enlarged view of the regional tetrahedral grids. Flexible refinement of different parts of the mantle is also supported. This workflow has been implemented into a separate meshing tool called Make3DModel. See main text for more detailed descriptions.

The step-by-step workflow is given as follows (see Figure 2):

- Step 1** Given the radius and global resolution of the spherical surface, generate a global uniform surface triangular mesh using STT (Figure 2a).
- Step 2** Given the coordinates of an observatory and its regional resolution, use STT's implementation to add polygon constraints to generate multi-resolution triangular mesh. Figure 2b shows an example of multi-resolution triangular mesh with two different resolutions, we call these two-level multi-resolution grids. Note that multi-level multi-resolution grids are also supported.
- Step 3** Given the radii, global, and regional resolutions of all surfaces, repeat steps 1 and 2 to generate multi-resolution triangular meshes (Figure 2c).
- Step 4** Construct solid model geometry and discretize it with multi-resolution tetrahedral grids using Gmsh (Figure 2d). We apply the Delaunay algorithm to generate high-quality tetrahedral meshes. Local refinement for 3D anomalies is also supported by specifying mesh element sizes. Finally, Figure 2e shows an enlarged view of the multi-resolution tetrahedral grids. The method developed in this study supports refinement for (1) downing to the entire mantle and (2) only the upper part of the mantle.
- Step 5** Set different physical attributes for surfaces and regions to impose boundary conditions and distribute conductivity values. Realistic conductivity distribution of the oceans and continents are interpolated into each element by spherical bilinear interpolation.

The above step-by-step workflow has been implemented into a separate meshing tool called Make3DModel. This tool supports the generation of both global uniform and multi-resolution tetrahedral grids.

### 2.2.2. Goal-Oriented h-Refinement Adapted for the Secondary Field Formulation

Given an initial mesh, the adaptive FE method solves the system of linear Equation 14 on a series of subsequently refined meshes to improve the accuracy. These subsequently refined meshes are obtained by refining a subset of elements. These elements are marked by an a-posterior error estimator.

Using the total electric field formulation, Ren et al. (2013) developed and tested several a-posterior error estimators and found that the error estimator based on the face-jumps of normal components of current density obtained the most robust performance. Using the idea of Ren et al. (2013), we adapt this error estimator for the secondary field formulation. Taking the divergence of Equation 7, we have

$$\nabla \cdot (\sigma \mathbf{E}_s + \delta\sigma \mathbf{E}_0) = 0, \quad (17)$$

which indicates that

$$\mathbf{n}_F \cdot [(\sigma^- \mathbf{E}_s^- + \delta\sigma^- \mathbf{E}_0^-) - (\sigma^+ \mathbf{E}_s^+ + \delta\sigma^+ \mathbf{E}_0^+)] = 0, \quad (18)$$

where the superscripts - and + denote different sides of interface  $F$  shared by two tetrahedra,  $\hat{\mathbf{n}}_F$  is the unit normal vector pointing from side - to side +. Due to the finite dimensional approximation, Equation 18 is not strictly satisfied, therefore, it can serve as an a-posterior error estimator

$$[\eta_K^e]^2 = \sum_{F \in \mathcal{F}(K)} \frac{1}{2} \|\mathbf{n}_F \cdot [(\sigma^- \mathbf{E}_s^- + \delta\sigma^- \mathbf{E}_0^-) - (\sigma^+ \mathbf{E}_s^+ + \delta\sigma^+ \mathbf{E}_0^+)]\|_{L^2(F)}^2, \quad (19)$$

where  $\eta_K^e$  is the error estimator of the  $K$ th tetrahedra,  $F$  is an interior face of  $\mathcal{F}(K)$ , which is the set of interior faces of the  $K$ th tetrahedra, the factor 1/2 comes from the fact that face  $F$  is shared by two tetrahedra, the  $L^2$  norm on face  $F$  reads

$$\|\cdot\|_{L^2(F)} = \left( \iint_F |\cdot|^2 \, ds \right)^{1/2}. \quad (20)$$

We are interested in obtaining accurate EM fields at specific measuring sites (subdomain of interest). This can be done by the goal-oriented adaptive mesh refinement technique, which needs to compute a dual field  $\mathbf{W}$  (also called influence function) by solving a dual boundary value problem (Ren et al., 2013).

$$\nabla \times \nabla \times \mathbf{W} + i\omega\mu_0\sigma\mathbf{W} = \frac{\gamma \mathbf{I}}{|\Omega_s|} \quad \text{in } \Omega, \quad (21)$$

$$\mathbf{e}_r \times \nabla \times \mathbf{W} = 0 \quad \text{at } \partial\Omega, \quad (22)$$

where  $\gamma$  is the characteristic function, which is equal to one only in the subdomain of interest ( $\Omega_s$ ), otherwise zero.  $|\Omega_s|$  is the volume of the subdomain of interest,  $\mathbf{I} = [1, 1, 1]$  is an artificially injected unit source located at a measuring site.

The error estimator for the dual field  $\mathbf{W}$  is denoted as  $\eta_K^w$ , which is computed according to Equation 19 by replacing  $\mathbf{E}_s^-$ ,  $\mathbf{E}_s^+$  with  $\mathbf{W}^-$ ,  $\mathbf{W}^+$ . When  $\eta_K^e$  is weighted by  $\eta_K^w$ , the final goal-oriented error estimator is defined as

$$\eta_K = \eta_K^e \eta_K^w. \quad (23)$$

With the availability of the error estimators (23) for all elements, a subset of elements with error indicator  $\eta_K$  satisfying

$$\frac{\eta_K}{\max(\eta_K)} = \beta_K > \beta, \quad 0 < \beta < 1, \quad (24)$$

are marked to be refined. Here  $\beta_K$  is the relative element error indicator and  $\beta$  is a given threshold value that controls the number of refined elements.

From a physical point of view, the artificially injected unit vector sources make the influence functions  $\mathbf{W}$  have a larger amplitude and vary more rapidly around the subdomain of interest than other domains. Therefore, the error

estimator  $\eta_K^w$  for the influence functions can be larger in the subdomain of interest, and weighing the electric field with influence functions by Equation 23 can enlarge the error estimator  $\eta_K$  around measuring sites.

### 2.2.3. Uniform p-Refinement on the Final Mesh

In the second step, we utilize high-order Nédélec elements (Nédélec, 1980) on the final mesh. When using the lowest-order tetrahedral Nédélec elements, there are six unknowns associated with six edges for each element. The high-order Nédélec elements assign more unknowns to each element to improve the accuracy. For a  $p$ th order tetrahedral Nédélec element, the total number of unknowns is (Nédélec, 1980)

$$N_u^p = \frac{p(p+2)(p+3)}{2}, \quad (25)$$

with  $6p$  unknowns are associated with edges,  $4p(p-1)$  unknowns are associated with faces, and  $p(p-1)(p-2)/2$  unknowns are associated with element interiors.

There is a consequence that the second order Nédélec elements can provide the best trade-off between the accuracy of solutions and computational efficiency for magnetotelluric and controlled-source EM problems (Castillo-Reyes et al., 2019; Grayver & Kolev, 2015). Therefore, we only test the second order elements for global EM forward modeling on tetrahedral grids.

### 2.2.4. Different Refinement Strategies

The automatic goal-oriented hp-adaptive refinement procedure is described as follows:

- Step 1** Generate an initial tetrahedral mesh according to the model geometry using the meshing tool developed in Section 2.2.1. Either uniform coarse or multi-resolution grids can be used.
- Step 2** Given the initial mesh, the iterations of adaptive mesh refinement  $N_{amr}$ , a maximum number of unknowns  $N_{dofs}$ , and the order  $p$  of finite elements for the final mesh, compute the FE solutions of the electric field  $\mathbf{E}_s$  and the dual field  $\mathbf{W}$  using the lowest-order edge-based Nédélec elements. Estimate the error indicator  $\eta_K$  for all elements by using the goal-oriented error estimator in Equation 23.
- Step 3** If the adaptive iteration number is less than  $N_{amr}$  and the current number of unknowns is less than  $N_{dofs}$ , mark the tetrahedra with error indicator  $\eta_K$  satisfying Equation 24, refine the marked tetrahedra by bisection algorithm (Arnold et al., 2000) to generate conforming tetrahedral grids, go back to step 2. Else go to step 4.
- Step 4** If the current number of unknowns is less than  $N_{dofs}$ , compute the FE solutions of the electric field  $\mathbf{E}_s$  using the  $p$ -order Nédélec elements. Go to step 5.
- Step 5** Compute the EM fields and response functions at measuring sites.

The global mesh refinement and the non-goal-oriented h-refinement are also implemented in our study. In summary, we implemented four adaptive FE methods, which are listed as follows:

- *Global mesh refinement*: Solve the electric field Equation 7 using the lowest-order Nédélec elements. Do not solve the dual Equation 21. Globally refine all tetrahedra by bisection.
- *Non-goal-oriented h-refinement*: Solve the electric field Equation 7 using the lowest-order Nédélec elements. Do not solve the dual problem 21. Locally refine the marked tetrahedra indicated by the *non-goal-oriented error estimator* in Equation 19.
- *Goal-oriented h-refinement*: Solve the electric field Equation 7 and the dual problem 21 using the lowest-order Nédélec elements. Locally refine the marked tetrahedra indicated by the *goal-oriented error estimator* in Equation 23.
- *Goal-oriented hp-refinement*: At  $N_{amr}$  adaptive iterations, solve the electric field Equation 7 and the dual problem 21 using the lowest-order Nédélec elements. Locally refine the marked tetrahedra indicated by the *goal-oriented error estimator* in Equation 23. At the last iteration, solve the electric field Equation 7 using the  $p$ -order Nédélec elements. When  $N_{amr} = 0$  and  $p = 1$ , this method reduces to the standard edge FE algorithm. When  $N_{amr} = 0$  and  $p > 1$ , this method is the high-order FE algorithm.

### 2.3. Efficiency Enhancement

An efficient linear solver and parallel implementation on distributed memory computers are lacking for the previous tetrahedral FE-based modeling solvers. We describe here the efficiency enhancements of our implementation briefly.

#### 2.3.1. Efficient Iterative Solvers

The FE approximations to global EM induction problems lead to a large system of linear equations with problem sizes commonly exceeding millions. Solving such a large system efficiently requires robust and scalable iterative linear solvers and preconditioners. To construct an efficient iterative solver, we split the complex-valued system of linear equations  $\mathbf{KU} = \mathbf{F}$  (Equation 14) into a  $2 \times 2$  block, real-valued linear system

$$\begin{pmatrix} \mathbf{S} & -\mathbf{M} \\ -\mathbf{M} & -\mathbf{S} \end{pmatrix} \begin{pmatrix} \mathbf{U}^R \\ \mathbf{U}^I \end{pmatrix} = \begin{pmatrix} \mathbf{F}^R \\ \mathbf{F}^I \end{pmatrix}, \quad (26)$$

where  $\mathbf{U}^R, \mathbf{U}^I$  denote the real and imaginary parts of the unknown electric field vectors. The explicit expressions in Equation 26 are  $S_{ij} = \iiint_{\Omega} (\nabla \times \mathbf{N}_i) \cdot (\nabla \times \mathbf{N}_j) dv, M_{ij} = \iiint_{\Omega} \omega \mu_0 \sigma \mathbf{N}_i \cdot \mathbf{N}_j dv, F_i^R = \iiint_{\Omega} \omega \mu_0 \delta \sigma \mathbf{N}_i \cdot \mathbf{E}_0^I dv, F_i^I = \iiint_{\Omega} \omega \mu_0 \delta \sigma \mathbf{N}_i \cdot \mathbf{E}_0^R dv$ , where  $\mathbf{E}_0^R$  and  $\mathbf{E}_0^I$  are the real and imaginary parts of the primary electric fields.

An optimal block-diagonal preconditioner for system 26 is (J. Chen et al., 2010)

$$\mathbf{P}_K = \begin{pmatrix} \mathbf{A} & \mathbf{0} \\ \mathbf{0} & \mathbf{A} \end{pmatrix}, \mathbf{A} = \mathbf{S} + \mathbf{M}. \quad (27)$$

The condition number of  $\mathbf{P}_K^{-1} \mathbf{K}$  has an upper bound of  $\sqrt{2}$  (J. Chen et al., 2010; Grayver & Kolev, 2015), therefore, iterative solvers can converge in a limited number of iterations. In this study, we adopt the FGMRES iterative algorithm (Saad, 2003) to solve Equation 26. The application of the block-diagonal preconditioner 27 to the FGMRES solver leads to two real-valued systems of linear equations with the same form:

$$\mathbf{Ax} = \mathbf{b}. \quad (28)$$

The linear system 28 can be solved using the preconditioned conjugate gradient (PCG) algorithm (Saad, 2003) with the auxiliary-space Maxwell solver (AMS) (Kolev & Vassilevski, 2009) as a preconditioner. The AMS can be also used as an iterative solver to solve Equation 28 directly. In summary, we implemented three iterative strategies to solve the linear systems 26 and 28:

- *FGMRES-AMS(1)*: The FGMRES solver is used to solve Equation 26 (outer iteration), and the AMS with only one iteration is used to solve Equation 28 (inner iteration). The FGMRES solver is terminated when a relative residual norm  $\|\mathbf{KU} - \mathbf{F}\|/\|\mathbf{F}\|$  of  $10^{-6}$  is reached. The parallel AMS (Kolev & Vassilevski, 2009) via hypre multigrid library (Baker et al., 2012) is adopted;
- *FGMRES-AMS*: Similar to FGMRES-AMS(1), but the AMS solver is terminated when a relative residual norm  $\|\mathbf{Ax} - \mathbf{b}\|/\|\mathbf{b}\|$  of  $10^{-2}$  or a maximum iteration of 20 is reached;
- *FGMRES-PCG*: The same FGMRES solver is used to solve Equation 26, but the PCG solver with one AMS circle is employed to solve Equation 28. The PCG solver is terminated when a relative residual norm  $\|\mathbf{Ax} - \mathbf{b}\|/\|\mathbf{b}\|$  of  $10^{-2}$  or a maximum iteration of 20 is reached.

Although the FGMRES-PCG strategy has been applied for magnetotelluric modeling on high-order hexahedral elements (Grayver & Kolev, 2015) and controlled-source EM modeling on the lowest-order edge-based tetrahedral elements (Qiu et al., 2021), it is necessary to further test the robustness of this strategy as well as two other strategies for global EM induction problems with respect to global source periods and high-order tetrahedral elements.

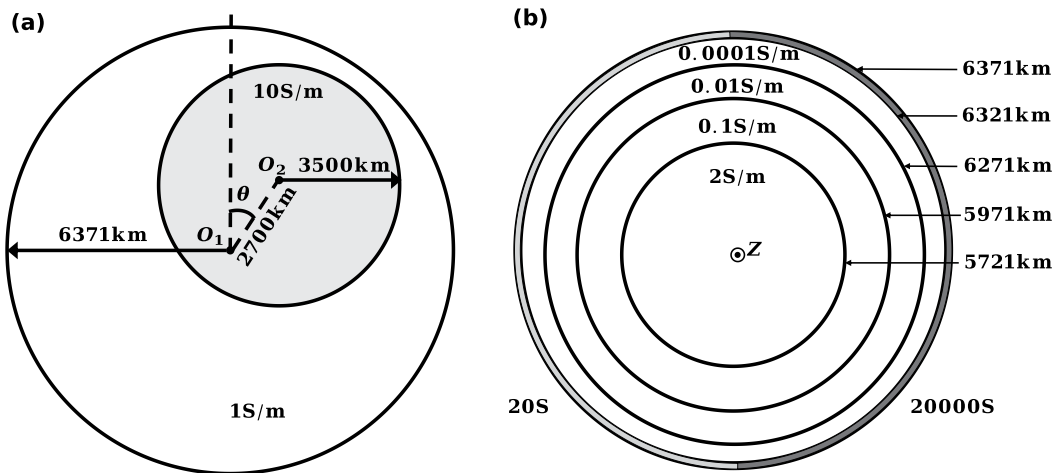


**Figure 3.** Synthetic global electrical conductivity models. (a) Cross-section along longitude  $\phi = 35^\circ$  of the nested sphere model (Martinec, 1998); (b) Illustration of the West-East hemisphere benchmark model (view down along the polar axis) (Kelbert et al., 2014). The surface conductance layer represents a synthetic conductivity distribution of oceans and continents.

### 2.3.2. Parallel Acceleration

To accelerate the computation, we adopt fully parallel implementation at both the frequency and mesh decomposition levels using MPI. As for parallelization at the frequency level, we split the total MPI processes into  $N_f$  groups, where  $N_f$  is the number of frequencies, and each group is responsible for one frequency. As for parallelization at the mesh decomposition level, assuming there are  $N$  MPI processes within each group, the whole computational domain is partitioned into  $N$  nonoverlapping, well-balanced subdomains using the METIS software (Karypis & Kumar, 1998), and each process owns one subdomain. Then we assemble the parallel system matrices based on the MFEM library (Anderson et al., 2021), compute the right-hand sides for the primal and dual problems, solve the system of linear equations, and do error estimation in parallel. Finally, for the post-processing, the EM fields and response functions at measuring stations owned by each MPI process are computed separately and parallelly, the root process receives, merges, and outputs the final solutions. Further efficiency enhancements include: (a) The relative tolerance for iteratively solving the dual problem 21 is set to a relaxed value of  $10^{-3}$  to reduce the number of iterations and computation time; (b) A refined mesh is shared by nearby frequencies, which can considerably reduce the computational requirements to perform adaptive mesh refinement.

## 3. Validation of Modeling Tool

We consider two synthetic models with totally different electrical structures (Figure 3) to validate the correctness of our method in handling both simple magnetospheric ring current and complex ionospheric Sq current sources as well as its accuracy and efficiency enhancements. The atmosphere conductivity was set to  $10^{-8}$  S/m for all simulations. The Earth's core was included in the models, so the boundary condition at the core-mantle boundary was not used. All computations were performed on a workstation with one Intel Xeon E5-2687W 3.10 GHz CPU and 220 GB RAM using 16 MPI processes unless otherwise stated.

### 3.1. Nested-Sphere Model

As the first example, we consider the nested sphere model of Martinec (1998) (Figure 3a). This model consists of a big sphere with a radius of 6,371 km and a conductivity of 1 S/m, and a small nested sphere with a radius of 3,500 km and a conductivity of 10 S/m. The small spherical inclusion is centered at radius  $r = 2,700$  km, colatitude  $\theta = 40^\circ$ , and longitude  $\phi = 35^\circ$ . The nested sphere model has been tested in a number of publications (Everett & Schultz, 1996; Kelbert et al., 2014; Ribaudo et al., 2012; Weiss & Everett, 1998). The solution of this model can be computed semi-analytically (Martinec, 1998). Therefore, this model is suitable for us to validate the accuracy of our solver.

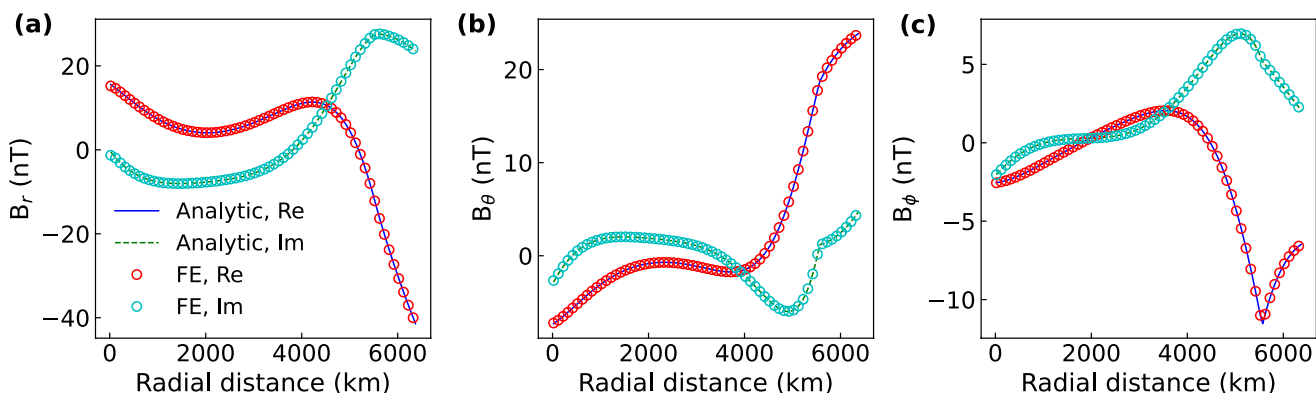


**Figure 4.** Comparison of our finite element solutions (symbols) with the semi-analytic solutions (lines) (Martinec, 1998) for (a) radial component  $B_r$ , (b) colatitudinal component  $B_\theta$ , and (c) longitudinal component  $B_\phi$  of magnetic field.

This model is excited by a  $Y_1^0 = \cos \theta$  magnetospheric ring current source with strength  $\epsilon_1^0 = 100$  nT. The excitation period is  $2.094 \times 10^7$  s as that in the study by Martinec (1998). The modeling domain was discretized with 201,454 tetrahedral elements. The mesh was locally refined along a radial measuring profile from the Earth's center to the surface with fixed colatitude  $\theta = 13^\circ$  and longitude  $\phi = 0^\circ$ . The element edge length near measuring stations is about 100 km. The second order finite elements were used for this run. The total computation time for this model with 2,564,848 unknowns and 16 MPI processes is only 68 s.

Figure 4 compares our FE solutions with the semi-analytic solutions (Martinec, 1998). Since the induced magnetic field is the main data source for global EM induction studies, we only show the solutions of the magnetic field. Excellent agreements are observed for three magnetic field components. For  $Y_1^0 = \cos \theta$  source structure, the  $B_\phi$  component was generated fully by the 3D nested sphere. A sharp change in  $B_\phi$  component near the boundary of the nested sphere is evident, which is in agreement with the analytic solutions. This test illustrates that our code can obtain accurate geomagnetic responses for a 3D conductivity model with subsurface structures of highly variable shape.

### 3.2. West-East Hemisphere Model

As the second example, we consider the West-East hemisphere benchmark model (Kelbert et al., 2014), which consists of a thin shell surface conductance and four layers underneath (Figure 3b). The surface conductance is 20S at longitudes 0–90° and 270–360°, and 20,000S at longitudes 90–270°. This model has been widely tested, and the sharp conductivity contrast and the thin shell structure are challenging for the tetrahedral FE approach. Therefore, this model is adopted to further test the correctness of our code. The modeling domain consists of 402,961 tetrahedral elements. The element edge length near measuring stations is 50 km (about 0.5° resolution). The second order elements were adopted with the number of unknowns being 5,116,976.

We first consider the  $Y_1^0$  magnetospheric ring current source with  $\epsilon_1^0 = 100$  nT. Three periods: 1 day, 4 days, and 16 days were tested. Note that although the conductivity structure of this model does not vary with colatitude  $\theta$ , the  $Y_1^0 = \cos \theta$  source structure makes the modeling setup fully 3D. We compare our FE solutions with IE solutions (Kuvshinov, 2008) in Figure 5. An overall good agreement is obtained for three magnetic field components. The main differences occur near the conductivity contrasts at longitudes 90° and 270°, which may be due to the different numerical discretizations of unstructured FE and structured IE methods. Results of  $B_r$  and  $B_\phi$  show sharp changes at longitudes 90° and 270°. These sharp changes reflect the large conductivity contrasts between the two hemispheres. With the increase of the periods, the field changes near conductivity contrast decrease. For a period of up to 16 days, the field changes due to the conductivity contrast become negligible.

We further check the capability of our code to handle ionospheric Sq current. A dominant spherical harmonic term  $Y_{k+1}^k$  with a unit source  $\epsilon_{k+1}^k = 1$  nT was considered for a period of  $\frac{24}{k}$  hours,  $k = 1, 2, 3, 4$ . The comparison of our FE solutions and IE solutions (Kuvshinov, 2008) is shown in Figure 6. Again, a good agreement between the two solutions is evident. This result validates the correctness of our code in handling ionospheric Sq current excitation. Compared to the case of magnetospheric ring current excitation, the shape of magnetic fields is much

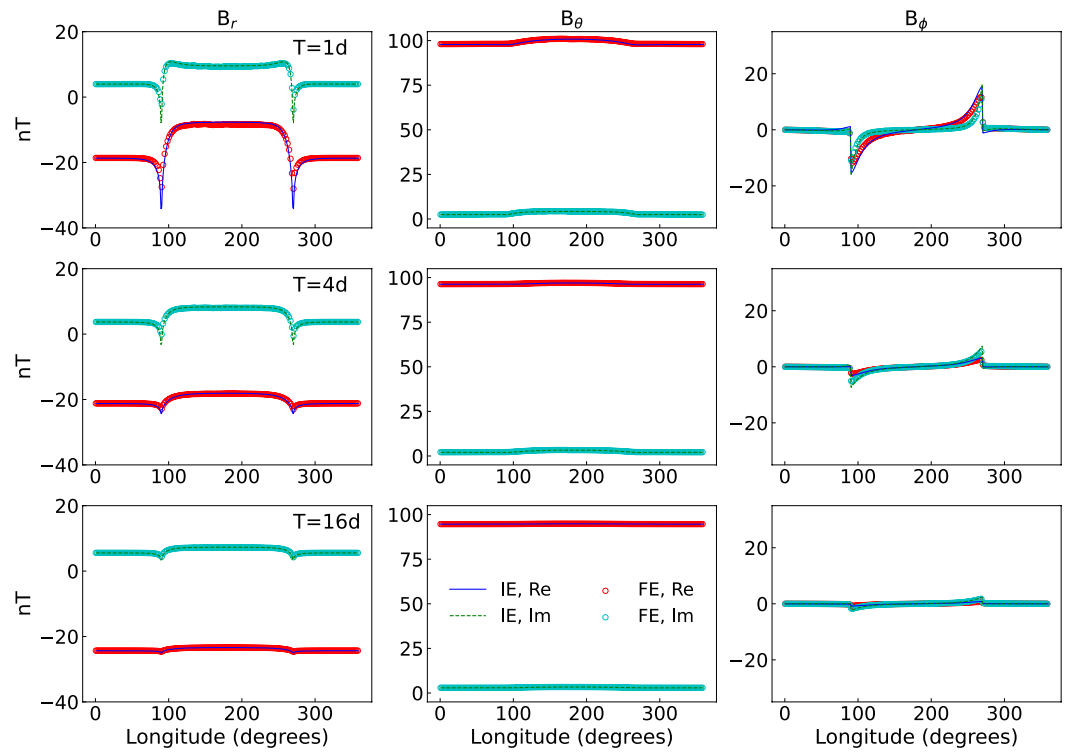


**Figure 5.** Comparison of our finite element solutions (symbols) with the integral equation solutions (lines) (Kuvshinov, 2008) for the West-East hemisphere model excited by the magnetospheric ring current. From the top to bottom rows, the corresponding periods are 1 day, 4 days, and 16 days, respectively. The measuring profile is located at Earth's surface with fixed colatitude of  $\theta = 45.5^\circ$ .

more complex, which is due to the complex structures of ionospheric Sq current. We also find that the sharp changes at longitudes  $90^\circ$  and  $270^\circ$  for the radial  $B_r$  and longitudinal  $B_\phi$  components are much more distinct. This is consistent with the fact, that the surface conductivity contrast affects the shorter period EM fields of ionospheric origin more than the longer period EM fields of magnetospheric origin.

This model has 5,116,976 unknowns, when using 16 MPI processes, the total computation time for a total of three magnetospheric periods is 789 s, while that is 1,272 s for a total of four ionospheric periods. Therefore, the solver takes only about 294 s (4.9 min) for one period. With the increase of MPI processes or using parallelization with respect to periods, the computation time can be further reduced. These results demonstrate that the FE-based forward modeling solver presented in this study has the capability of computing accurate multi-source EM responses in a few minutes on parallel computing platforms.

### 3.3. Tests of Accuracy Enhancement

Having tested the correctness, we now test the performance of accuracy improvement by using different adaptive refinement strategies. The nested sphere model (Figure 3a) was tested. The initial coarse mesh has 136,210 tetrahedral elements. During adaptive mesh refinement, elements with  $\beta_K > \beta = 0.05$  are marked to be refined in the next iteration.

We check the convergence rate of implemented adaptive methods by plotting the average relative difference versus the number of unknowns and the total run time. The average relative difference for the magnetic fields is defined as

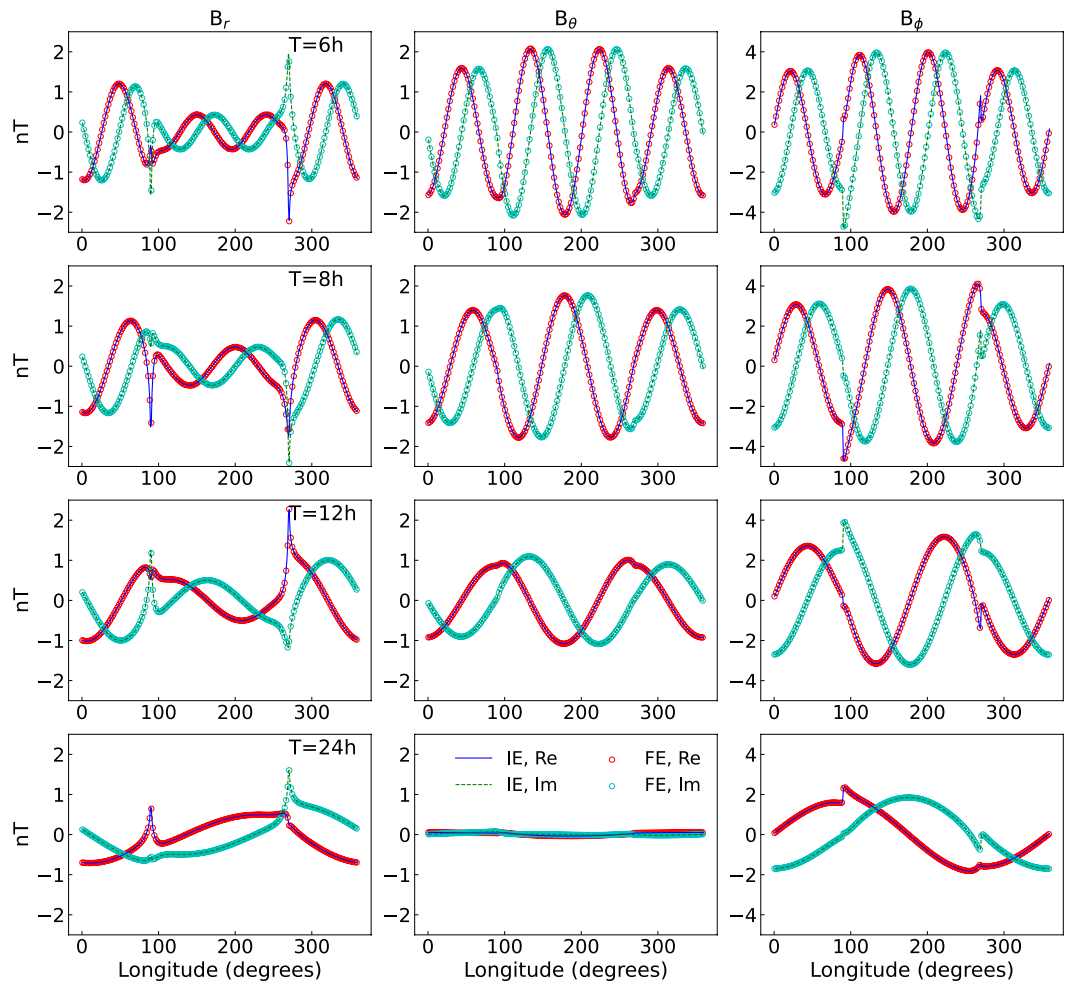


**Figure 6.** Similar to Figure 5, but for the ionospheric Sq current. From the top to bottom rows, the corresponding periods are 6, 8, 12, and 24 hr, respectively.

$$\text{Relative difference} = \frac{\sqrt{\sum_{j=1}^N |B_j^{fem} - B_j^{ref}|^2}}{\sqrt{\sum_{j=1}^N |B_j^{ref}|^2}} \times 100\%, \quad (29)$$

where  $N$  is the total number of measuring magnetic fields, which can be either  $B_r$  or  $B_\theta$  or  $B_\phi$ . The superscripts *fem* and *ref* denote our FE solutions and the semi-analytic solutions of Martinec (1998), respectively.

We first discuss the results of three fully h-refinement approaches that adopt the lowest order elements, which are the global mesh refinement, non-goal-oriented h-refinement, and goal-oriented h-refinement. As shown in Figure 7, the theoretically optimal convergence rate for h-refinement using the linear finite elements is  $-1/3$  (Brenner & Scott, 2008). Neither the global mesh refinement nor the non-goal-oriented h-refinement obtains (Ribaudo et al., 2012) this optimal rate. Instead, the goal-oriented h-refinement using linear elements demonstrates a super-optimal convergence rate because both regions with sharp variations of conductivities and around receiver sites have been optimally refined (Figures 8e and 8f). We should note that the solutions of the goal-oriented h-refinement approach at the seventh iteration are more accurate than the final solutions of global mesh refinement and non-goal-oriented h-refinement approaches. The corresponding number of unknowns is only 1,020,244, which is about 20 times less than 20,403,188 of the global mesh refinement technique and about 16 times less than 16,782,352 of the non-goal-oriented h-refinement technique. The computation time for the

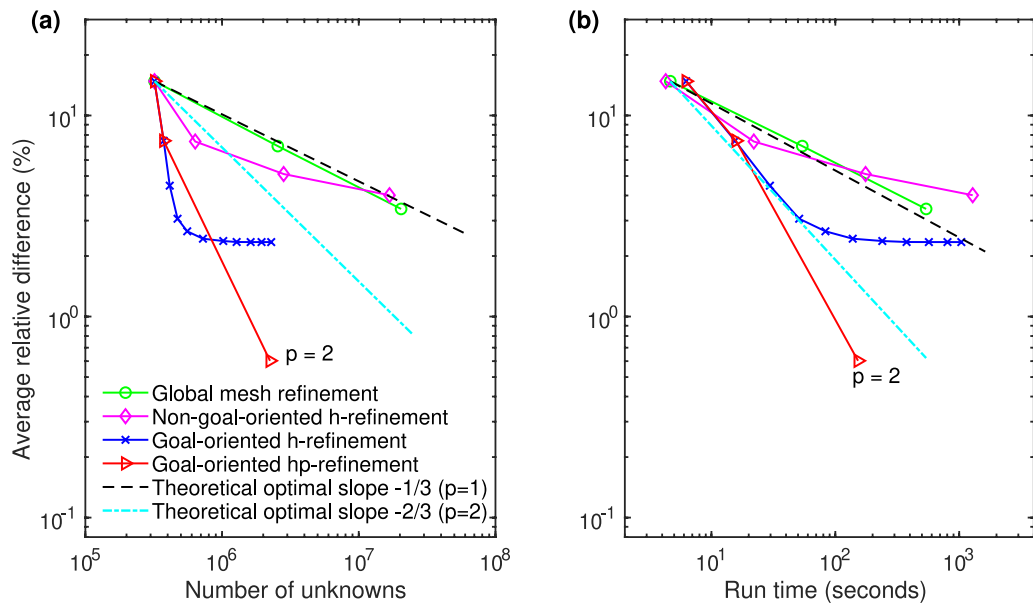


**Figure 7.** Convergence of the relative difference versus the number of unknowns and the total run time for the implemented adaptive finite element strategies tested on the nested sphere model (Figure 3a). For the goal-oriented hp-refinement approach, the second order Nédélec elements were used on the final mesh. The black and cyan dash lines indicate the theoretically obtainable optimal convergence curves of the h-refinement approach, with a log-log slope of  $-1/3$  for the lowest order elements and  $-2/3$  for the second order elements (Brenner & Scott, 2008).

goal-oriented h-refinement is also considerably shorter. These results clearly demonstrate that the goal-oriented h-refinement approach can offer highly accurate solutions even with a much less number of unknowns and shorter computation time.

We now discuss the results of the goal-oriented hp-refinement. If using the second-order elements, the expected optimal convergence rate for the h-refinement approach is  $-2/3$  on a log-log plot (Brenner & Scott, 2008). The results shown in Figure 7 indicate that the slope of the goal-oriented hp-refinement technique is steeper than  $-2/3$ . The relative difference of the goal-oriented hp-refinement technique reduces more than one order of magnitude, with less number of unknowns and shorter computation time compared to the goal-oriented h-refinement. These results highlight the accuracy and efficiency of the goal-oriented hp-refinement strategy.

To see the details of adaptive refinement procedures, we show in Figure 8 the mesh density and the relative element error indicators  $\beta_K$  (see Equation 24) of the third adaptive grids generated by the implemented adaptive refinement strategies. Starting from an initial coarse mesh with 136,210 tetrahedra, the third refined mesh of the global mesh refinement technique has 8,717,440 tetrahedra and 2,040,3188 unknowns. We observe that meshes have been refined globally for elements both near and far away from the measuring profile (white dash line). The averaged relative difference of measuring sites of this solution is 3.43%, which is close to that of the solution at the third iteration for the goal-oriented h-refinement approach with fewer unknowns (414,316), only 2% of those used in the global mesh refinement. As shown in Figures 8e and 8f, the goal-oriented h-refinement approach has efficiently identified and refined the subdomain of interest that includes the measuring profile. In the meanwhile, the elements far away from the measuring profiles are not noticeably refined. This is due to the fact that once the global mesh density reaches a certain level, the accuracy of measuring sites is mainly dependent on the local mesh densities (Brenner & Scott, 2008). The mesh is shown in Figures 8g and 8h has the same density as that in Figures 8e and 8f, but shows lower relative element error indicators due to the use of the second order elements. This result also indicates that with the goal-oriented hp-refinement strategy, we can obtain highly accurate solutions.

When utilizing the secondary field approach, the small nested sphere is a heterogeneous body with respect to the background Earth, induced currents are generated within the nested sphere. Therefore, the secondary field in and close to anomalies will vary sharply. This can enlarge the error estimator  $\eta_K^e$  (see Equation 19) for the secondary electric field in the nested sphere. In this case, the non-goal-oriented h-refinement approach driven by the

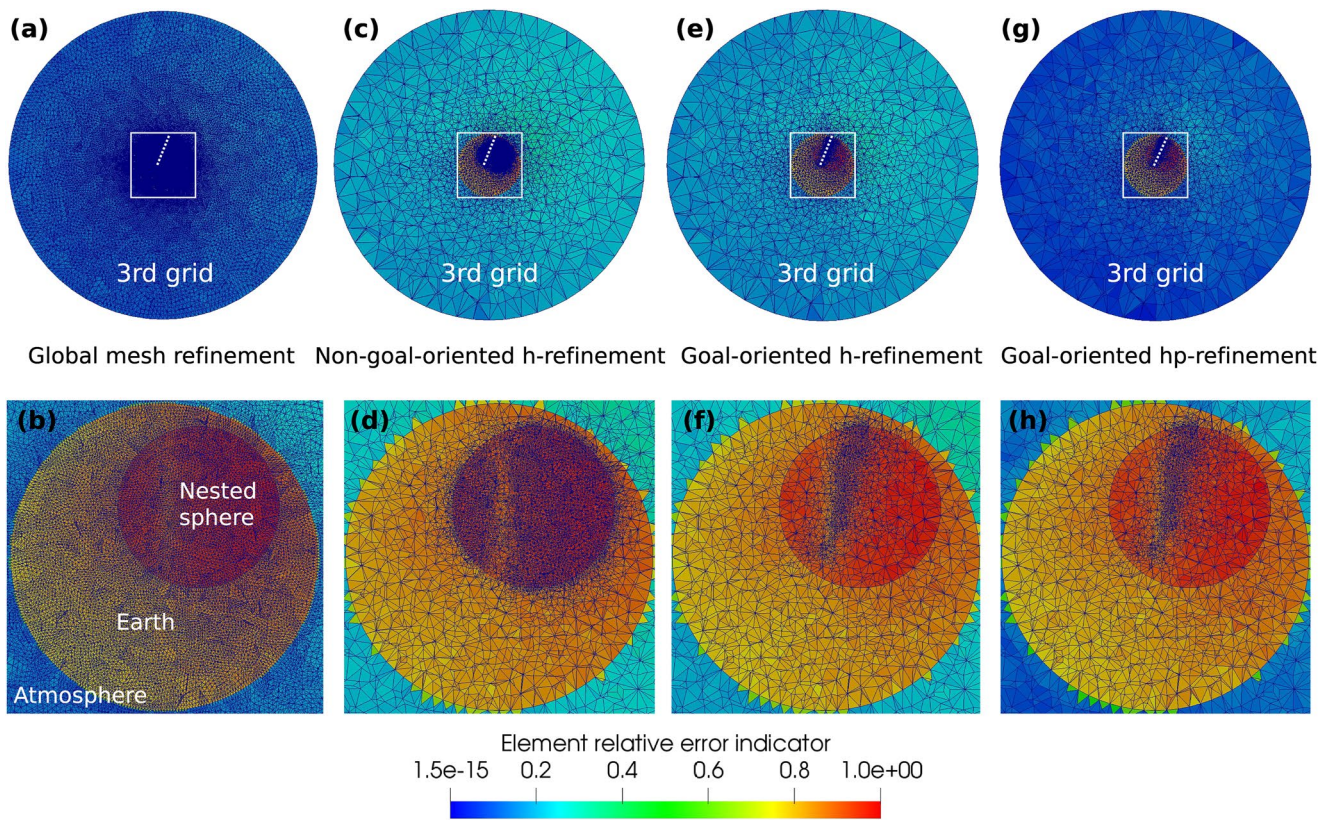


**Figure 8.** Mesh density and element relative error indicator  $\beta_K$  of the third grids generated by (a) (b) the global mesh refinement; (c) (d) the non-goal-oriented h-refinement; (e) (f) the goal-oriented h-refinement; and (g) (h) the goal-oriented hp-refinement for the nested sphere model (Figure 3a). Top and bottom rows denote the global and local enlarged views for the white rectangle, respectively. The white dash line denotes the measuring profile.

non-goal-oriented error estimator  $\eta_K^e$  will mainly refine the elements in and close to the nested sphere. Numerical experiments for the non-goal-oriented h-refinement approach as shown in Figures 8c and 8d verify this theoretical analysis. We also observe that the non-goal-oriented h-refinement approach as applied for global EM forward modeling utilizing tetrahedral grids (Ribaudo et al., 2012) fails to identify the subdomain of interest that includes the measuring profile. This result is in agreement with the poor convergence rate of this approach (Figure 7).

### 3.4. Tests of Efficiency Enhancement

As described in Section 2.3.1, our modeling tool employs three iterative strategies: FGMRES-AMS(1), FGMRES-AMS, and FGMRES-PCG, where FGMRES denotes the outer iteration, AMS and PCG denote the inner preconditioning iteration. Here we test the efficiency and robustness of these strategies with respect to periods dominated by global magnetospheric ring current (from 4 to 128 days) and ionospheric Sq current (from 6 hr to 1 day). The second-order tetrahedral Nédélec elements were used. The tetrahedral meshes have 201,454 and 402,961 elements for the nested sphere and West-East hemisphere models, respectively.

Table 1 lists the number of iterations and computation time of three different iterative strategies for the nested sphere model (Figure 3a). We observe that the number of FGMRES iterations and computation time for FGMRES-AMS(1) strategy increase only slightly with respect to periods. For FGMRES-AMS and FGMRES-PCG strategies, the number of FGMRES iterations is robust with respect to periods. The computation time increases slightly due to the increase of inner AMS or PCG iterations. These results suggest a good performance of all iterative strategies for this model.

However, the results are different for the more complex West-East hemisphere model (Figure 3b). As shown in Table 2, we find that: (a) The number of iterations and computation time for the FGMRES-AMS(1) solver increase rapidly and change with periods significantly. This result shows that using only one AMS circle for

**Table 1**

Comparison of Different Iterative Strategies on the Number of Iterations and Computation Time (in Seconds) for the Nested Sphere Model at Both Ionospheric (From 6 hr to 1 day) and Magnetospheric (From 4 to 128 days) Period Ranges

Period	FGMRES-AMS(1)		FGMRES-AMS			FGMRES-PCG		
	$N_{iter}^{fgmres}$	Time	$N_{iter}^{fgmres}$	$\bar{N}_{iter}^{ams}$	Time	$N_{iter}^{fgmres}$	$\bar{N}_{iter}^{pcg}$	Time
6 hr	28	25	16	3	38	16	3	49
8 hr	28	25	16	3	38	16	3	47
12 hr	28	25	16	3	38	16	3	48
1 day	26	24	16	3	35	16	3	49
4 days	24	23	16	2	32	16	4	50
16 days	26	25	16	3	37	16	4	52
64 days	28	27	16	3	42	16	4	52
128 days	30	28	16	4	49	16	4	53

Note. This simulation was performed using the second order tetrahedral Nédélec elements and 16 MPI processes.  $N_{iter}^{fgmres}$  denotes the number of iterations of outer FGMRES solver,  $\bar{N}_{iter}^{ams}$  denotes the inner number of AMS circles averaged for  $N_{iter}^{fgmres}$  times FGMRES iterations,  $\bar{N}_{iter}^{pcg}$  denotes the inner number of PCG iterations averaged for  $N_{iter}^{fgmres}$  FGMRES iterations. The number of elements and unknowns are 201,454 and 2,564,848, respectively.

preconditioning is not robust for solving global EM forward problems. (b) For the FGMRES-AMS and FGMRES-PCG solvers, the number of FGMRES iterations increases only slightly, demonstrating the robustness of these two strategies. The computation time increases noticeably, which is due to the increase in the number of elements and inner AMS or PCG iterations.

By testing three iterative strategies for models with totally different electrical structures, we recommend using the most robust FGMRES-PCG solver for complex models with large conductivity contrast and thin shell structures (such as the West-East hemisphere model), and the fastest FGMRES-AMS(1) solver for models with simpler structures (such as the nested sphere model) to accelerate computation. To make our modeling tool more flexible and efficient, in our implementation, these three iterative strategies can be set freely.

### 3.5. Tests of Parallel Acceleration

Solving the large-scale linear systems efficiently is the major bottleneck of global EM induction modeling and inversion, therefore we focus on testing the scalability of the iterative solver with the FGMRES-AMS(1) strategy as an example. The nested sphere model (Figure 3a) with a period of  $2.094 \times 10^7$  s was tested. Using the first order Nédélec elements, three uniform refined meshes were designed: the first-mesh has 736,874 tetrahedra and

**Table 2**

Similar to Table 1, but for the West-East Hemisphere Model

Period	FGMRES-AMS(1)		FGMRES-AMS			FGMRES-PCG		
	$N_{iter}^{fgmres}$	Time	$N_{iter}^{fgmres}$	$\bar{N}_{iter}^{ams}$	Time	$N_{iter}^{fgmres}$	$\bar{N}_{iter}^{pcg}$	Time
6 hr	115	166	20	14	391	18	8	194
8 hr	112	164	20	14	381	18	8	196
12 hr	106	155	20	13	351	18	8	197
1 day	98	146	18	12	303	18	8	207
4 days	120	178	18	19	412	18	10	235
16 days	152	229	18	19	475	18	11	259
64 days	168	253	18	20	499	18	11	266
128 days	172	260	16	20	445	18	11	276

Note. The number of elements and unknowns are 402,961 and 5,116,976, respectively.

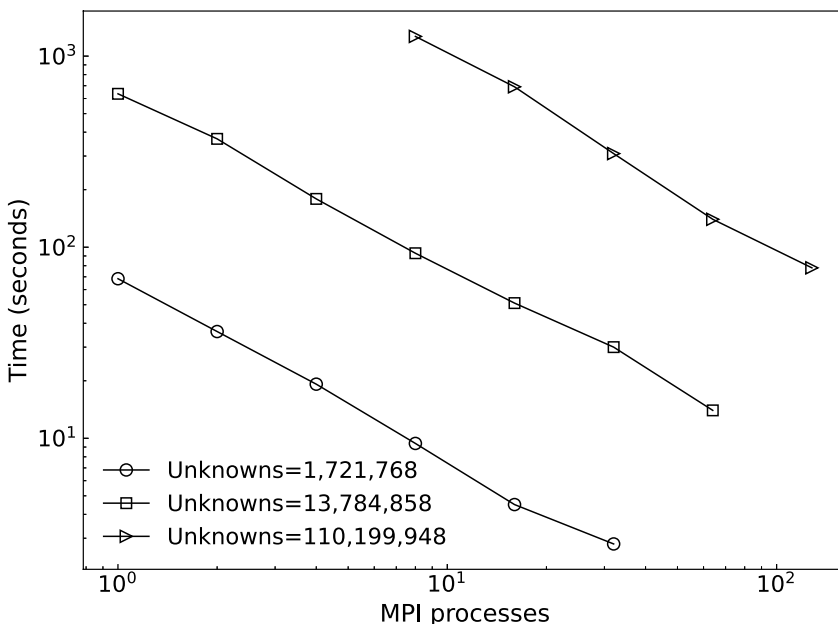


**Figure 9.** Computation time for solving the system of linear equations versus the number of MPI processes for different number of unknowns. The proportionally decreased computation time demonstrates the efficiency of the iterative solver.

1,721,768 unknowns, the second-mesh has 5,894,992 tetrahedra and 13,784,858 unknowns, the third-mesh has 47,159,936 tetrahedra and 110,199,948 unknowns. The simulations were performed in the High-Performance Computing Center of Central South University. This platform has a total of 1,022 distributed nodes, each node is equipped with two Intel Xeon Gold 6248R 3.0 GHz CPUs, 48 cores, and 192 GB RAM.

Figure 9 illustrates the computation time versus the number of MPI processes for three tests with an increased number of unknowns. The minimum run time (maximum number of MPI processes) for solving the system of linear equations is only about 3 s (32 processes) for about 1 million unknowns, 14 s (64 processes) for 10 millions unknowns, and 78 s (128 processes) for 100 millions unknowns, respectively. We also observe that the computation time decreases proportionally to the MPI processes, indicating the strong scalability of the solver. These results demonstrate that our code has the capability of fast dealing with global EM induction problems with a large number of unknowns. Further efficiency tests of our FE code on a realistic problem will be reported in the remaining sections.

#### 4. Interpretation of Chinese Coastal Geomagnetic Observatory Data

##### 4.1. Background

China has a long coastline (Figure 10b), which is surrounded by active subduction zones. The subducted Pacific and Philippine Sea plates have played important roles in the tectonic evolution of eastern China. The water in the subducted oceanic slabs can be carried into the mantle transition zone and the lower mantle (Karato, 2011). A small amount of water can significantly affect the physical and chemical properties of mantle minerals, such as plastic deformation (Mei & Kohlstedt, 2000) and the melting temperature (Kushiro et al., 1968). Therefore, constraining the amount and distribution of water in the mantle transition zone beneath China plays an important role in understanding the dynamics and evolution of continental China.

Chinese coastal geomagnetic observatory data provides a unique data source to study the water content of the Pacific and Philippine Sea subduction zones. Recently, the coastal geomagnetic data in northeast China have been used to constrain the mantle electrical conductivity and water content (Y. Zhang et al., 2020). However, several coastal geomagnetic observatories in southeast China (such as Quanzhou and Yongning observatories) are not used for mantle conductivity imaging (Yuan et al., 2020) due to the lack of accurately accounting for the strong local ocean effects.

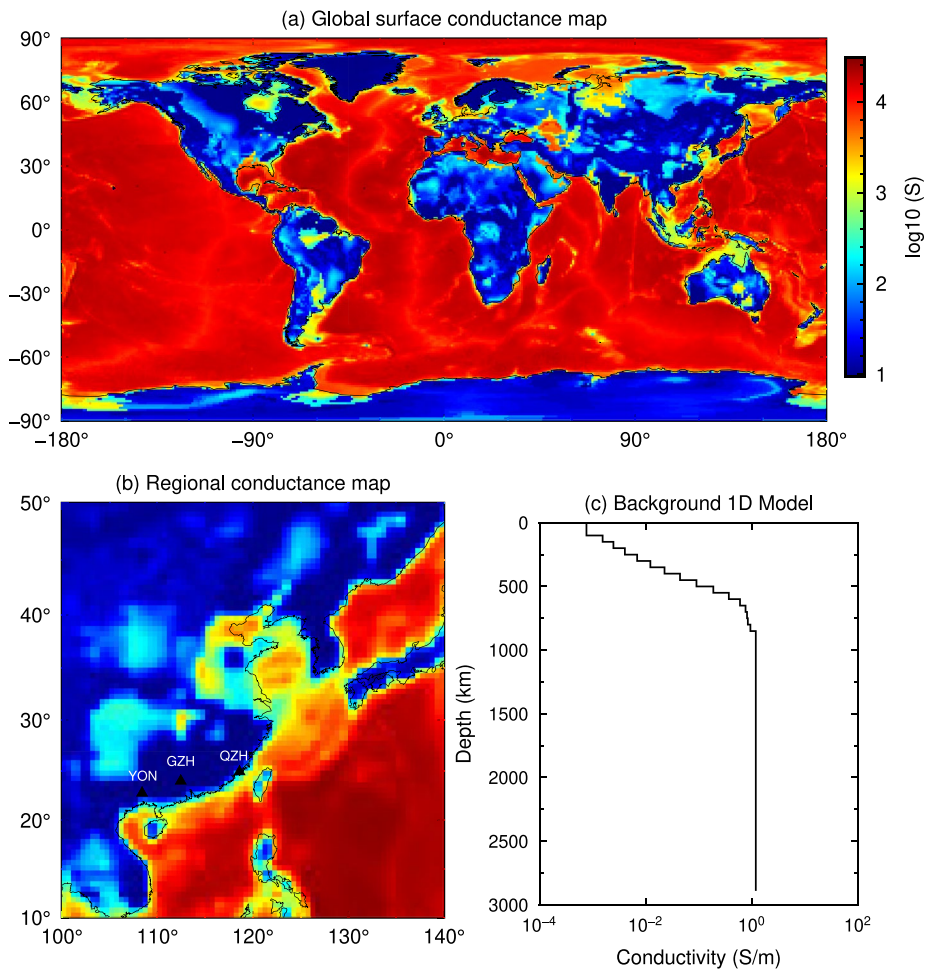


**Figure 10.** Realistic 3D conductivity model includes near-surface conductive heterogeneities and an underlying 1D mantle conductivity structure. (a) Global surface conductance map representing the nonuniform distributions of oceans and continents with  $0.5^\circ \times 0.5^\circ$  resolution. (b) Enlarged regional conductance map near China. Three coastal Chinese observatories are marked by black triangle, with corresponding information recorded in Table 3. (c) 1D mantle conductivity model beneath the north Pacific derived by Shimizu, Koyama, et al. (2010).

We now apply our multi-resolution finite element approach to guide the interpretation of the southeast China coastal observatory data. Does this application aim to answer the following questions: (a) How does the ocean affect the responses from coastal geomagnetic observatories in China? (b) How dense the resolution of the surface layer is needed to accurately model the local ocean effects? (c) Will inaccurate correction for the ocean effects lead to a large difference among inverse conductivity profiles? (d) Is the transition zone wet or dry beneath southeast China?

#### 4.2. Data and Inversion

Since we mainly aim to constrain the transition zone electrical conductivity and water content beneath southeast China, we only consider the geomagnetic variations from 2 to 108 days, which are dominated by the  $Y_1^0$  magnetospheric ring current (Banks, 1969; Kelbert et al., 2008; Kuvshinov, 2012). In this case, we work with the geomagnetic depth sounding (GDS)  $C$ -response (Banks, 1969)

$$C(\mathbf{r}_a, \omega) = -\frac{a \tan \theta_d}{2} \frac{B_r(\mathbf{r}_a, \omega)}{B_{\theta_d}(\mathbf{r}_a, \omega)}, \quad (30)$$

**Table 3**

*Selected Coastal Observatories in Southeast China With Geographic (GG) and Geomagnetic (GM) Latitude and Longitude Are Recorded in Degrees*

Code	Observatory	GG latitude	GG longitude	GM latitude	GM longitude	Data length
QZH	Quanzhou	24.90	118.60	14.60	189.53	2009–2017
GZH	Guangzhou	23.97	112.45	13.54	183.78	1961–1979
YON	Yongning	22.76	108.40	12.30	179.97	1995–2007

*Note.* Data length denotes the time series length of hourly mean value of geomagnetic fields used to estimate observed C-responses.

where  $\mathbf{r}_a = (a, \theta, \phi)$  is the location of a given geomagnetic observatory at Earth's surface,  $\theta_d$  is the geomagnetic colatitude,  $B_r$  is the radial component of the magnetic field and  $B_{\theta_d}$  is the geomagnetic south component of the magnetic field.

Three coastal geomagnetic observatories in southeast China are analyzed: Quanzhou (QZH), Guangzhou (GZH), and Yongning (YON). The GZH observatory has been used in previous 1D GDS studies (Shimizu, Koyama, et al., 2010; Utada et al., 2003), while the QZH and YON observatories have not been analyzed for mantle induction studies. The locations of selected observatories are shown in Figure 10b, with detailed information, are listed in Table 3. The observed C-responses are estimated from the hourly mean value of geomagnetic fields following the method of Semenov and Kuvshinov (2012). Data uncertainty is estimated by jackknife approach (Chave & Thomson, 1989).

The large conductivity contrast between oceans and continents can distort the geomagnetic responses (Kuvshinov et al., 2002; C. Chen et al., 2020). After removal of the surface ocean effects using 3D modeling results, as discussed later, the corrected C-responses are inverted for probing the 1D reference mantle conductivity. The 1D conductivity model from Earth's surface to the core mantle boundary is discretized into a total of 40 layers. The thickness of each layer is 50 km at depths less than 1,000 km, while that is 100 km at depths from 1,000 km to the core mantle boundary (2,890 km). A high conductivity value of  $1 \times 10^5$  S/m is set for the Earth's core.

We search for the mantle conductivity model by minimizing the following objective function

$$\phi(\mathbf{m}, \lambda) = \phi_d(\mathbf{m}) + \lambda \phi_m(\mathbf{m}) \rightarrow \min, \quad (31)$$

where  $\phi_d(\mathbf{m})$  is the data misfit term,  $\phi_m(\mathbf{m})$  is the model regularization term that controls the smoothness of conductivities between adjacent layers (Constable et al., 1987),  $\lambda$  is the regularization parameter used to balance the data misfit and the smoothness of inverse conductivity models,  $\mathbf{m}$  is the model vector that consists of the logarithmic electrical conductivity, that is  $\mathbf{m} = [\log(\sigma_1), \log(\sigma_2), \dots, \log(\sigma_{N_m})]$ , with  $\sigma_i$  being the conductivity of the  $i$ -layer and  $N_m$  being the number of layers.

The data misfit term is defined as the difference between predicted and observed responses weighted by data uncertainties

$$\phi_d(\mathbf{m}) = \sum_{i=1}^{N_d} \frac{|C^{\text{obs, corr}}(\mathbf{r}_a, \omega_i) - C^{\text{pred}}(\mathbf{r}_a, \omega_i, \mathbf{m})|^2}{(\delta C^{\text{obs}}(\mathbf{r}_a, \omega_i))^2}, \quad (32)$$

where  $N_d$  is the total number of data for the observatory located at  $\mathbf{r}_a = (a, \theta, \phi)$ ,  $C^{\text{obs, corr}}(\mathbf{r}_a, \omega_i)$  is the observed C-response corrected for the ocean effects with  $\delta C^{\text{obs}}(\mathbf{r}_a, \omega_i)$  being the corresponding data uncertainty.  $C^{\text{pred}}(\mathbf{r}_a, \omega_i)$  is the predicted C-response, which is computed analytically using the recursive formulation of Kuvshinov and Semenov (2012) for a given 1D forward model  $\mathbf{m}$ . The root mean square (RMS) data misfit is computed by

$$\text{RMS} = \sqrt{\phi_d/N_d}. \quad (33)$$

The model regularization term is defined as the logarithmic conductivity difference between adjacent layers

$$\phi_m(\mathbf{m}) = \sum_{i=2}^{N_m} (m_i - m_{i-1})^2, \quad (34)$$

where  $N_m$  is the number of layers,  $m_i = \log(\sigma_i)$  is the logarithmic conductivity.

The inverse problem 31 is solved by the L-BFGS algorithm (Nocedal & Wright, 2006). A set of independent inversions are performed with a fixed value of  $\lambda$ , the final  $\lambda$  is determined by L-curve analysis (Hansen, 1992). The initial conductivity model is set to 1 S/m.

#### 4.3. Investigation of Ocean Effects Using Multi-Resolution Modeling Tool

Before inverting the observed data for the subsurface mantle conductivity structures, we first investigate the near-surface ocean effects on the coastal observatories in southeast China. We use a 3D conductivity model that consists of a heterogeneous surface conductance map at the top 10 km and a 1D reference conductivity profile underneath (Figure 10) to compute 3D  $C$ -responses. The surface conductance map (Figure 10a) was constructed following the method of Everett et al. (2003), and the crust, sediment, and ocean conductivity models have been updated. The CRUST1.0 model (Laske et al., 2013) was taken as the base model whose sediment layers were updated from the global 5 arc min sediment model GlobSed (Straume et al., 2019). The 3D ocean conductivity model (Tyler et al., 2017) was then used. Our surface conductance model has a resolution of  $0.5^\circ \times 0.5^\circ$ . This conductance map was also interpolated into  $1^\circ \times 1^\circ$ ,  $2^\circ \times 2^\circ$ , and  $4^\circ \times 4^\circ$  resolutions. The conductance maps were then transformed into conductivities. For the unstructured tetrahedral meshes used here, the conductivity of each surface tetrahedral grid was obtained by spherical bilinear interpolation (Y. Zhang et al., 2018). For the underlying 1D mantle structure, we use the averaged 1D mantle conductivity model (Figure 10c) beneath the North Pacific derived by Shimizu, Koyama, et al. (2010). This model is chosen as it is close to our study region. We will discuss this issue in more detail later.

We design five cases to verify our multi-resolution modeling approach and investigate the local ocean effects: (a) **global4deg**: use finite-element mesh and surface conductance map of global uniform  $4^\circ$  angular resolution; (b) **global2deg**: use finite-element mesh and surface conductance map of global uniform  $2^\circ$  angular resolution; (c) **global1deg**: use finite-element mesh and surface conductance map of global uniform  $1^\circ$  angular resolution; (d) **regional1deg**: use finite-element mesh and surface conductance map of  $1^\circ$  angular resolution in a region of  $20^\circ \times 20^\circ$  around the geomagnetic observatory, and  $2^\circ$  angular resolution elsewhere; (e) **regional0.5deg**: use finite-element mesh and surface conductance map of  $0.5^\circ$  angular resolution in a region of  $20^\circ \times 20^\circ$  around the geomagnetic observatory, and  $2^\circ$  angular resolution elsewhere.

For global modeling, the results of three geomagnetic observatories were simulated simultaneously by a common mesh. For regional modeling, we used independent multi-resolution mesh for each observatory to better account for the local ocean effects. Figure 11 shows an example of the multi-resolution mesh for the GZH observatory. The mesh has an angular resolution of  $1^\circ$  in a region of  $20^\circ \times 20^\circ$  around the geomagnetic observatory, and  $2^\circ$  angular resolution elsewhere. Elements near the coastline of this region were refined.

A total of 15 equally logarithmic spaced periods from 2 to 108.625 days were used to compute the local  $C$ -responses. We compared the results on the initial grid and the adaptively refined grid. Small differences (less than 1%) were found as the initial grid is good enough and elements near the observatories have been efficiently refined. Therefore, we use the initial grid in the following examples. All computations were performed on a workstation using 16 MPI processes. The detailed computation parameters are recorded in Table 4. The number of FGMRES iterations is not sensitive to the number of unknowns and different mesh resolutions. For global modeling, with the increase in the global resolution, the number of unknowns and computation time increases rapidly. Compared to the global1deg resolution, we observe that the number of unknowns and computation time of multi-resolution regional1deg reduce by a factor of about three. For the case of regional1deg, the total run time for 15 periods is, respectively, 48.6, 50.7, and 46 min for QZH, GZH, and YON observatories. The average time for 15 periods is 48 min, with 3.2 min for one period. For a 3D model with a similar but rather simpler structure, the computation time of the widely used IE code (Kuvshinov, 2008) was reported to be approximately 2 min for one period (Kelbert et al., 2014). Note that since our FE code can run on distributed memory computers,

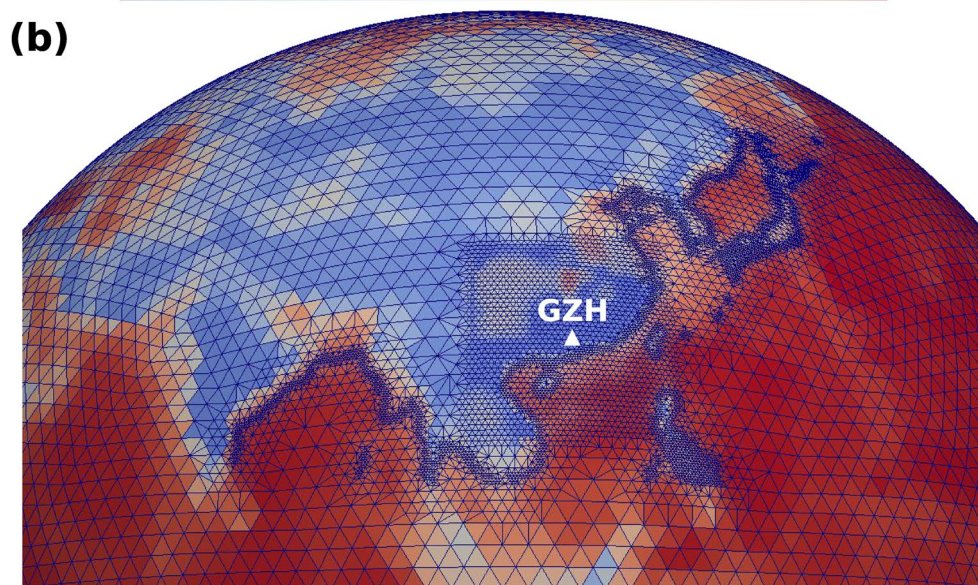
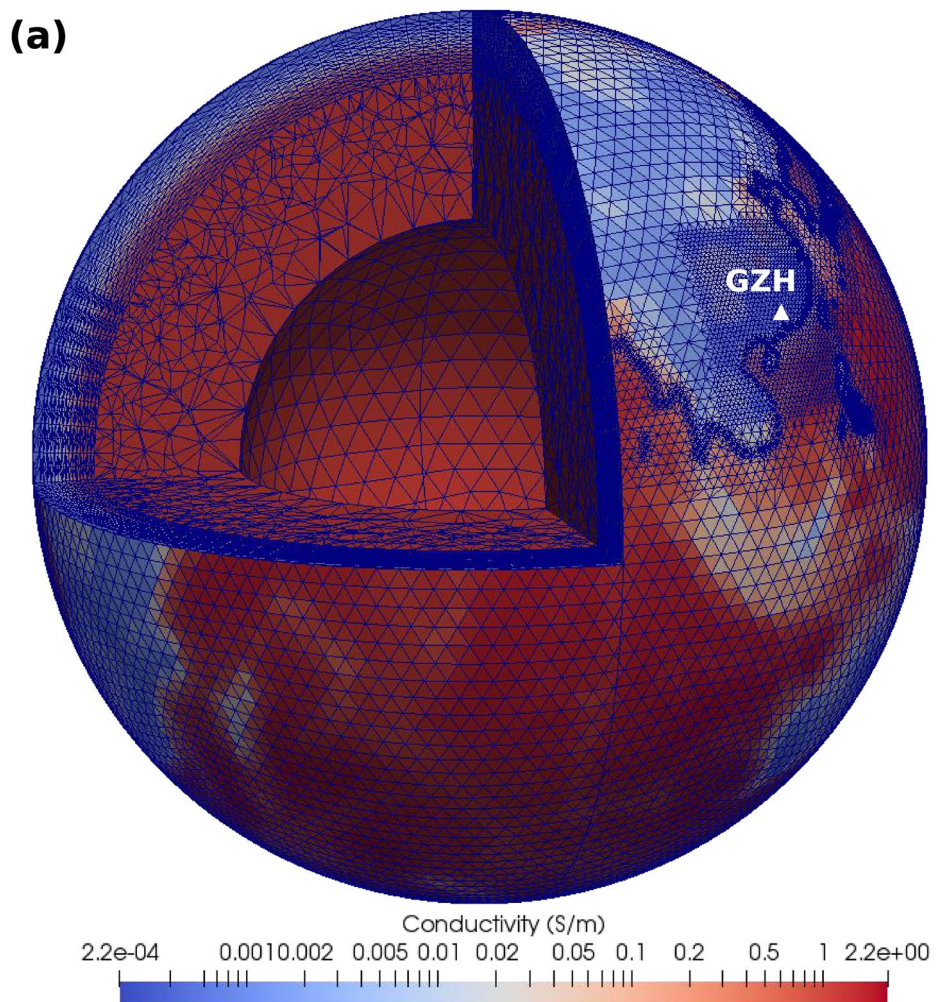


**Figure 11.** Global (a) and local (b) views of the multi-resolution tetrahedral grids with  $1^\circ$  angular resolution around GZH coastal observatory and  $2^\circ$  angular resolution globally.

**Table 4**

*Number of Unknowns, Number of FGMRES Iterations Averaged for 15 Periods, and Total Computation Time (in Seconds) of Global and Multi-Resolution Modeling for QZH, GZH, and YON Observatories*

Resolution	QZH			GZH			YON		
	Unknowns	Iter	Time	Unknowns	Iter	Time	Unknowns	Iter	Time
global4deg	1,107,918	19	940	1,107,918	19	940	1,107,918	19	940
global2deg	3,527,642	18	2,370	3,527,642	18	2,370	3,527,642	18	2,370
global1deg	13,146,158	18	8,754	13,146,158	18	8,754	13,146,158	18	8,754
regional1deg	4,102,476	18	2,917	4,082,290	18	3,043	4,047,666	18	2,760
regional0.5deg	7,103,400	18	5,576	6,487,662	18	4,785	6,595,392	18	4,711

*Note.* This simulation was performed using the first order Nédélec edge elements and 16 MPI processes.

the computation time can be further reduced by applying more MPI processes and multi-frequency parallelization. Therefore, our solver can work equally efficiently for realistic problems compared to the IE code.

Figure 12 shows the modeled  $C$ -responses of different resolution grids for QZH, GZH, and YON observatories. For comparison, the  $C$ -responses for the background 1D mantle conductivity model without surface ocean layer are also shown. For a 1D model, the imaginary parts of  $C$ -responses should be negative for a time-harmonic factor of  $e^{i\omega t}$  and show a substantial decrease with increasing periods (Semenov & Kuvshinov, 2012). However, compared to the 1D responses, the modeled 3D  $C$ -responses show significant differences at short periods, indicating the strong influence of the ocean. The real part of  $C$ -responses provides the estimation of the penetration depth of EM fields at a given period (Weidelt, 1972). Due to the shielding attenuation of high conductors, when modeling with conductive oceans, the real part of 3D  $C$ -responses will be smaller at short periods compared to 1D responses. This is consistent with our modeling results. This result suggests that inversion of uncorrected observed  $C$ -responses would obtain spurious more conductive upper mantle structures.

We observe that the results of 4 and  $2^\circ$  resolutions show distinct differences compared to those of 1 and  $0.5^\circ$  resolutions, especially for the imaginary parts. The  $C$ -responses have no significant changes when the resolution is finer than  $1^\circ$ , suggesting that a conductance map with a resolution finer than  $1^\circ \times 1^\circ$  is adequate to account for the ocean effects on coastal observatories in southeast China. The overall agreements between results of global1deg and regional1deg validate the correctness and accuracy of the multi-resolution approach. The small differences are due to the different ways of generating surface mesh. For global modeling, the surface meshes were generated by Gmsh (Geuzaine & Remacle, 2009) directly for convenience. For multi-resolution modeling, the surface meshes were generated using STT (Y. Zhang et al., 2018).

With the availability of 3D multi-resolution modeling results of local ocean effects. The observed  $C$ -responses are corrected for the near-surface ocean effects using the following method (Kuvshinov et al., 2002; Utada et al., 2003)

$$C^{\text{obs, corr}}(\mathbf{r}_a, \omega) = C^{\text{obs}}(\mathbf{r}_a, \omega) \cdot \frac{C^{\text{1D}}(\mathbf{r}_a, \omega)}{C^{\text{3D}}(\mathbf{r}_a, \omega)}, \quad (35)$$

where  $C^{\text{obs, corr}}(\mathbf{r}_a, \omega)$  are the observed  $C$ -responses corrected for the ocean effects,  $C^{\text{obs}}(\mathbf{r}_a, \omega)$  are the uncorrected observed  $C$ -responses,  $C^{\text{1D}}(\mathbf{r}_a, \omega)$  and  $C^{\text{3D}}(\mathbf{r}_a, \omega)$  denote the modeled  $C$ -responses for the background 1D model without and with the surface heterogeneous layer.

Figure 13 shows the uncorrected and corrected  $C$ -responses using modeling results of different resolutions. We find that the real parts of the  $C$ -responses do not increase with the increase of periods, which may indicate the existence of strong 3D anomalies at the middle to lower mantle related to the subducted slabs near these areas (Fukao et al., 2009). Another possible reason for this anomalous behavior may be the violation of  $Y_1^0$  source structure at low geomagnetic latitude (Fujii & Schultz, 2002; Semenov & Kuvshinov, 2012). As the periods increase, the uncertainty of data increases, this is due to the short data length used to estimate the responses. To obtain more reliable observed responses, more longer and continuous time series of the magnetic fields are needed in the future. We note that the correction of the ocean effects leads to very different responses, especially

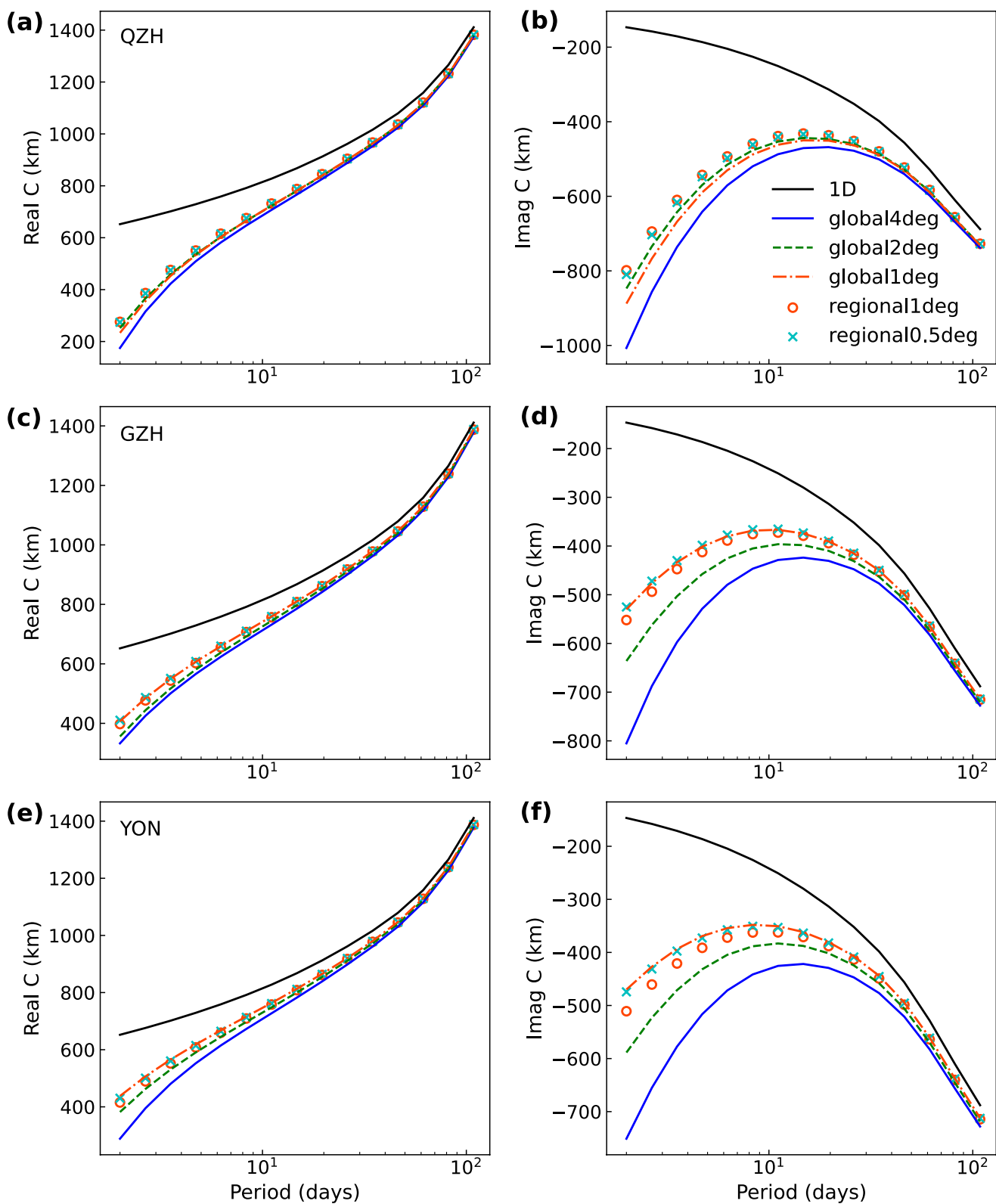


**Figure 12.** Real (left) and imaginary (right) parts of local C-responses simulated by multi-resolution finite-element approach for (a) (b) QZH; (c) (d) GZH; (e) (f) YON observatories. The C-responses of the background 1D mantle conductivity model without surface ocean layer are shown in black line.

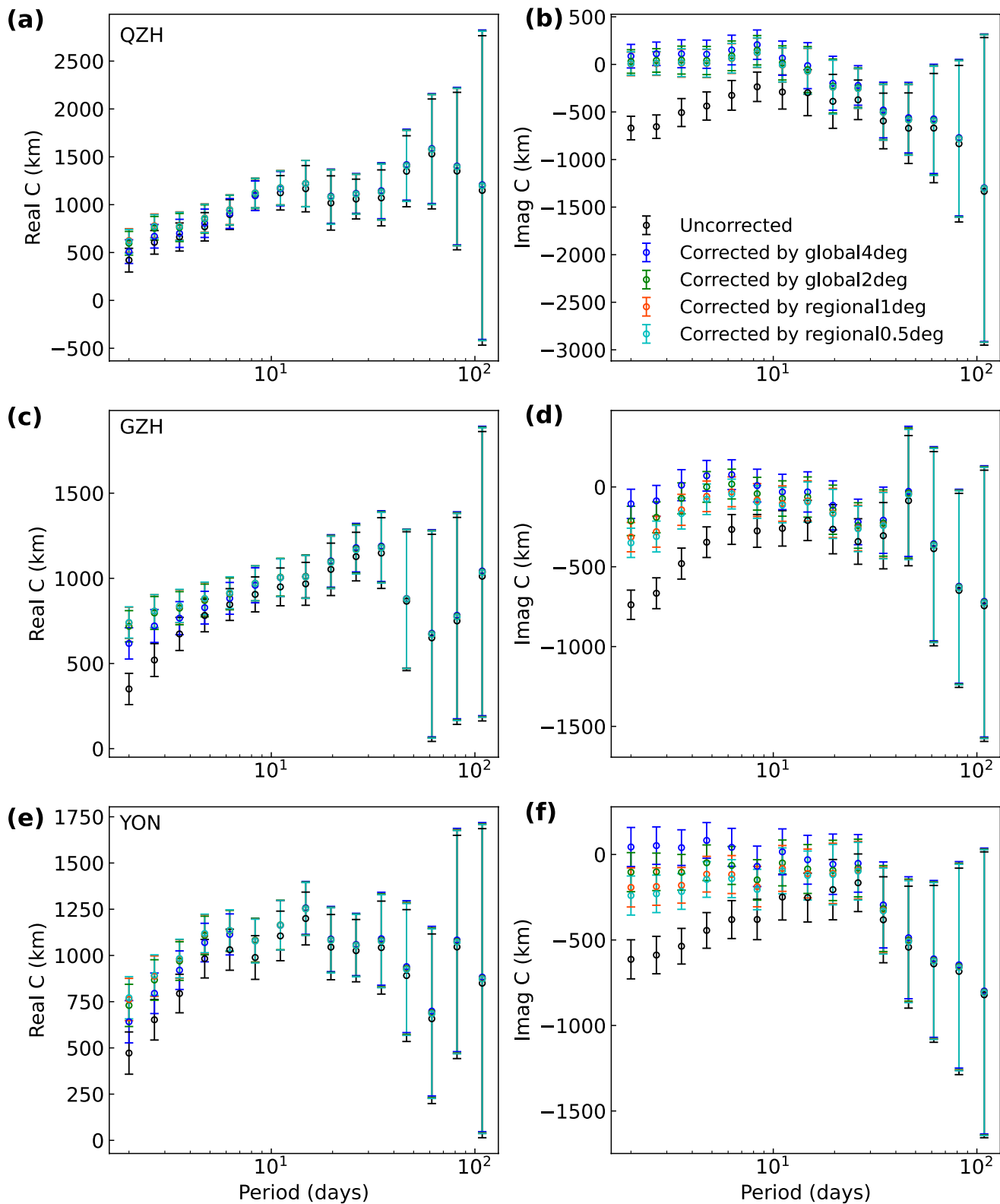


**Figure 13.** Real and imaginary parts of observed  $C$ -responses corrected for ocean effects using modeling results of different resolutions for (a) (b) QZH; (c) (d) GZH; (e) (f) YON observatories.

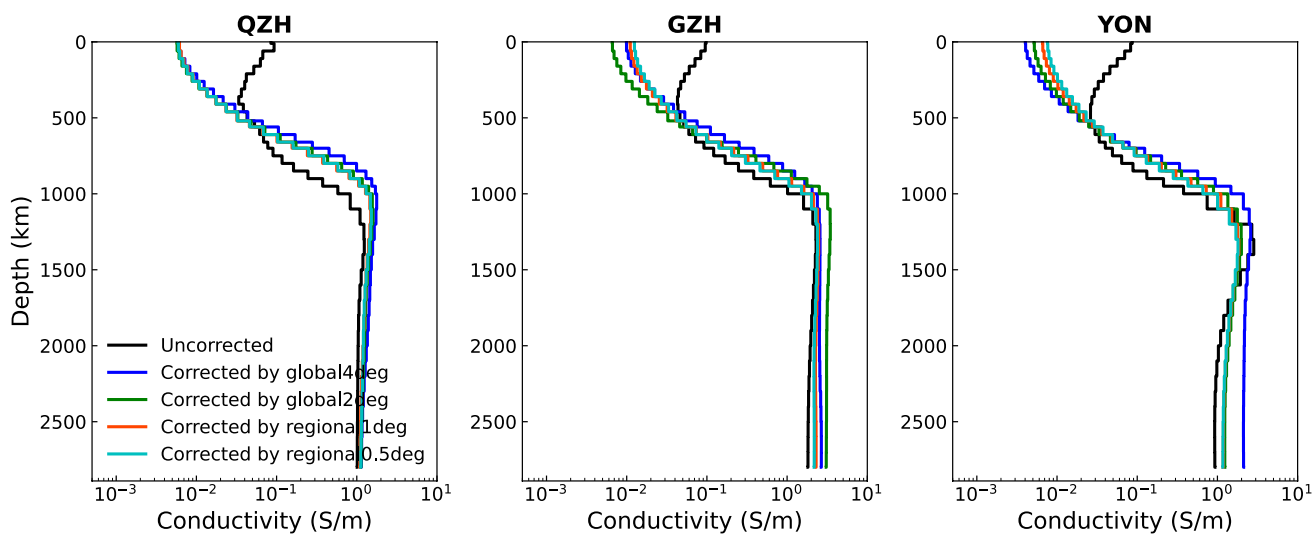


**Figure 14.** Inverted conductivity models for QZH, GZH, and YON observatories obtained by correcting ocean effects with multi-resolution results.

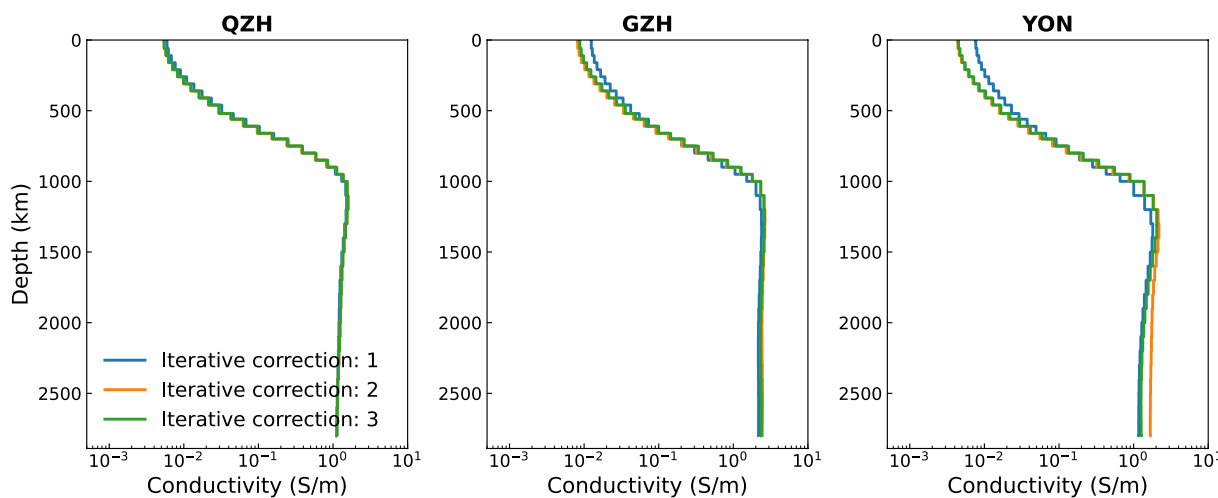
for the imaginary parts at periods shorter than 10 days. We also observe that the imaginary parts of the responses corrected by modeling results of 4° resolution show several positive values at short periods, which is not consistent with 1D responses. This result suggests that inaccurate modeling of the ocean effects can lead to wrong corrected responses.

We now check if inaccurate correction for the ocean effects will lead to large differences among inverse conductivity models. Figure 14 shows the inverse conductivity models obtained by correcting ocean effects with multi-resolutions results. For comparison, we also show the models obtained by inverting uncorrected responses. For all observatories, the models obtained by inverting the uncorrected and corrected responses show large differences in the upper mantle. The conductivity differences can reach one order of magnitude. After correction for the ocean effects, the inverse conductivity models are more resistive in the upper mantle, which is in agreement with the finding of Kuvshinov and Olsen (2006). These results also indicate that the *C*-responses are sensitive to upper mantle conductivity, although they have limited resolution in the upper mantle.

For the QZH observatory, when corrected by modeling results of 4° resolution, the conductivity model does not show distinct differences from those of finer resolution. This is in agreement with the fact that the differences in corrected responses of different resolutions are within the data uncertainties (Figures 13a and 13b). However, for the GZH and YON observatories, distinct differences are observed among inverse conductivity models. This is due to the large differences among corrected responses (Figures 13c–13f). Note that the conductivity differences can occur even in the lower mantle for the YON observatory. These results show that inverting inaccurate corrected responses can lead to spurious conductivity structures. This spurious solution can propagate from the upper to lower mantle. Therefore, it is better to adopt a mesh with a resolution of 1° or finer to account for the local ocean effects.

#### 4.4. Conductivity Models

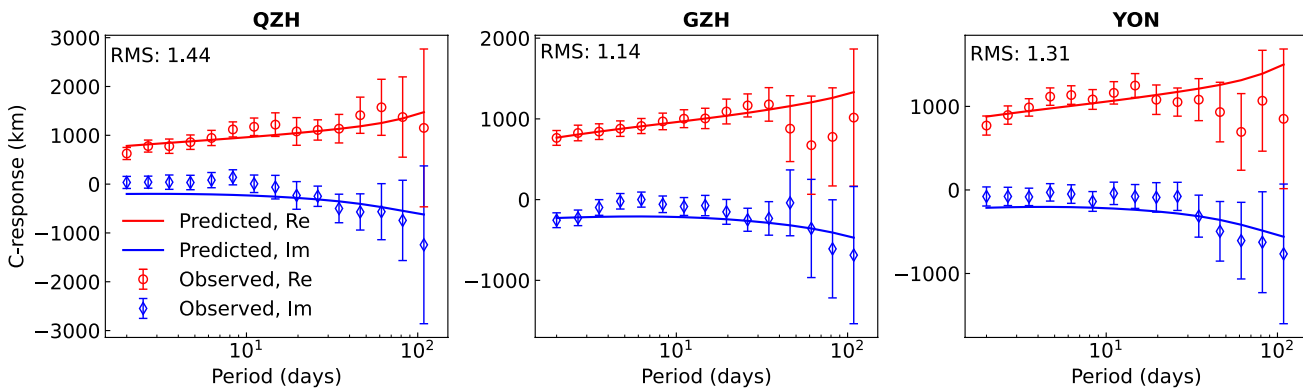
The 1D mantle conductivity profile used for ocean effects correction may have considerable effects on the inverse conductivity models. To obtain reliable conductivity models and reduce the computational requirements, we make the correction and inversion iterated as adopted by several previous studies (Kuvshinov et al., 2005; Shimizu, Koyama, et al., 2010; Utada et al., 2003). The 1D model beneath the north Pacific (Shimizu, Koyama, et al., 2010) is used for ocean effects correction and inversion at the first iteration. Then the inverse conductivity model is used for ocean effects correction and inversion at the next iteration. This procedure is iterated until there is no significant change in conductivity or a maximum iteration is reached. During this procedure, the 0.5° resolution was adopted for accurately modeling the local ocean effects.



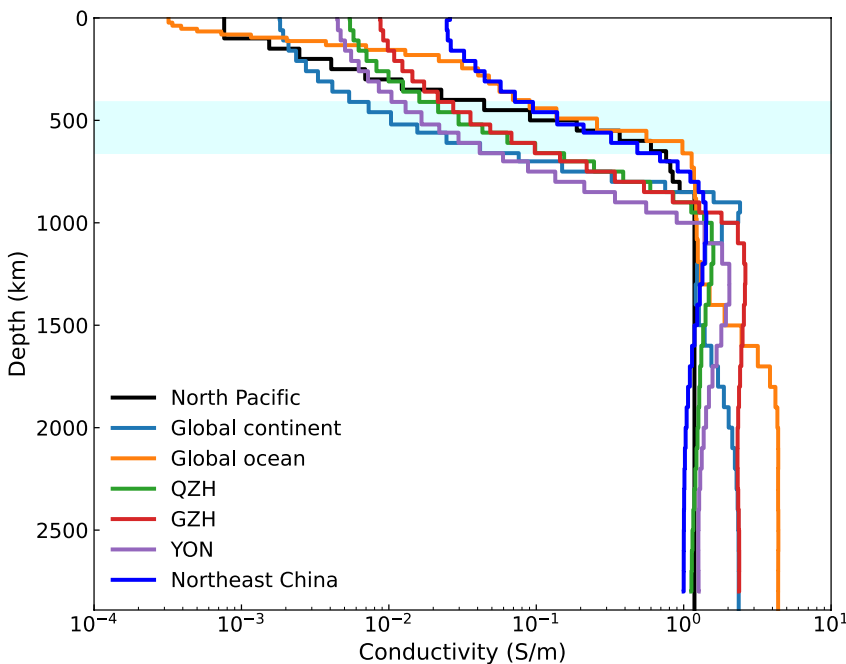
**Figure 15.** Inverted conductivity models for QZH, GZH, and YON observatories obtained by iterative ocean effect correction.

Figure 15 compares the inverse conductivity models of different iterative corrections. The conductivity models beneath QZH observatory have no distinct changes, indicating the relatively small local ocean effects. We note that making the correction and inversion iterated generates distinct differences among conductivity models beneath GZH and YON observatories. After three iterative corrections, this procedure converges and the conductivity models become slightly more resistive in and above the mantle transition zone. The conductivity models at the third iteration are taken for further analysis. The corresponding predicted and corrected observed  $C$ -responses are shown in Figure 16. A RMS value of 1.14 is obtained for the GZH observatory, indicating that the 1D model beneath this observatory can explain the data well. Slightly larger RMS of 1.44 and 1.31 are obtained for QZH and YON observatories. For the QZH observatory, this may be due to the complex 3D heterogeneities related to the subducted slabs of this region (Fukao et al., 2009), in which case the 1D assumption is not valid and a 3D inversion is needed. For the YON observatory, this is likely related to the Hainan mantle plume as revealed by seismic study (Wei & Chen, 2016) or source effect from equatorial electrojet. These issues will be discussed in future work.

The final 1D conductivity profiles for QZH, GZH, and YON observatories are shown in Figure 17. Two distinct features are observed. First, all models show a monotonic increase from the surface to about 1,200 km, followed by a roughly constant conductivity value down to the core-mantle boundary. The roughly constant value in the lowermost part may be attributed to the reduced resolution of GDS data. Second, conductivity jumps at main mineral phase transition depths (410, 520, and 660 km) are not resolved by our data, which is due to the diffusion nature of EM fields and the use of smoothness constraints. To generate structurally sparse models, one can adopt



**Figure 16.** Final predicted and corrected observed  $C$ -responses for QZH, GZH, and YON observatories. Error bars denote uncertainties of estimated  $C$ -responses.



**Figure 17.** Final conductivity models for QZH, GZH, and YON observatories. Their geographic locations are shown in Figure 10b, with corresponding observatory details, are listed in Table 3. For comparison, the average 1D model beneath north Pacific (Shimizu, Koyama, et al., 2010), the global model of Püthe et al. (2015), which mainly denotes average continent structure, and the global model of Kuvshinov et al. (2021), which mainly denotes average oceanic structure, and the conductivity model beneath northeast China (beneath Changchun (CNH) observatory) is also shown. The mantle transition zone is marked by a shaded area.

the  $L_1$ -norm regularization (Grayver et al., 2017) or release the smoothness constraint at these depths (Shimizu, Koyama, et al., 2010; Utada et al., 2003).

#### 4.5. Comparison With Previous Conductivity Models

Several global and semi-global 1D conductivity models (Kuvshinov et al., 2021; Püthe et al., 2015; Shimizu, Koyama, et al., 2010) are also plotted in Figure 17. We first compare our models with two oceanic mantle conductivity models. One is the average conductivity model beneath the north Pacific (Shimizu, Koyama, et al., 2010) (denoted as ‘North Pacific’). This model was obtained by inverting the semi-global submarine cable magnetotelluric responses and GDS responses of North Pacific, including the responses from the GZH observatory. The other is the global oceanic model (Kuvshinov et al., 2021), which was derived by jointly inverting satellite detected magnetospheric and tidal magnetic signals. This model is mainly an average of global oceanic conductivity structure and is denoted as ‘Global ocean’. Above the transition zone, our models are more conductive than the north Pacific model by more than one order of magnitude. Compared to the global oceanic model (Kuvshinov et al., 2021), our models are more conductive at depths less than 100–150 km, suggesting a more conductive continental lithospheric and asthenospheric mantle than that beneath the ocean. In the mantle transition zone, our models are more resistive by more than half an order of magnitude. We now compare our models with the global model of Püthe et al. (2015), which was obtained by inverting global observatory and satellite magnetic data. This model reflects mainly the conductivity structure of the continent and therefore is denoted as a ‘Global continent’. The comparison reveals that the upper mantle and transition zone beneath southeast China are more conductive than those of the global continental mantle.

For comparison, the conductivity model beneath northeast China (Figure 17) was also obtained by inverting the geomagnetic data from Changchun (CNH) observatory using the same method. We observe that the model beneath northeast China is more conductive than that beneath southeast China by more than half an order of magnitude. This result is consistent with previous low-resolution global and semi-global 3D conductivity models (Fukao et al., 2004; Kelbert et al., 2009; Li et al., 2020; Semenov & Kuvshinov, 2012; Shimizu, Utada,

et al., 2010; Sun et al., 2015) of this region. The high conductivity anomaly in the mantle transition zone beneath Changchun observatory was also reported in a previous GDS study (Ichiki et al., 2001) and was attributed to the water in the stagnant slab.

#### 4.6. Implications for Transition Zone Water Content

The conductivity of mantle minerals can be expressed as a function of temperature and water content (Karato, 2011; Yoshino, 2010). If the mantle temperature structure is known, we can estimate the water content in the mantle by comparing geophysical inverse conductivity models with the laboratory conductivity results. During the last two decades, the effects of water on mantle minerals have been measured under high temperature and high-pressure conditions (Karato, 2011; Yoshino, 2010). However, among these research groups, the effects of water on the conductivity of mantle minerals are considerably different. To avoid biases in the estimation of water content, we adopted the laboratory conductivity data of two groups: (a) Karato and coworkers; (b) Yoshino and coworkers.

The laboratory conductivity-depth profiles were constructed following the methods of Karato (2011) and Yoshino (2010), the latest adiabatic mantle temperature profile (Katsura, 2022) was assumed. We consider the main minerals in the mantle. For the laboratory conductivity models of Karato and coworkers, the laboratory data of Wang et al. (2006) was used for olivine in the upper mantle (above 410 km), and the data of Dai and Karato (2009) was used for wadsleyite in the upper transition zone (410–520 km), and the data of X. Huang et al. (2005) was used for ringwoodite in the lower transition zone (520–660 km). For the laboratory conductivity models of Yoshino and coworkers, laboratory data for olivine, wadsleyite, and ringwoodite were taken from Yoshino et al. (2009), Yoshino and Katsura (2012), and Yoshino et al. (2008), respectively.

The comparison of our inverse models with the laboratory conductivity models is shown in Figure 18. Using the laboratory data of Karato and coworkers, the water content in the mantle transition zone beneath northeast and southeast China is slightly less than 0.1 wt% and 0.01 wt%, respectively, indicating that the mantle transition zone beneath southeast China is drier compared to northeast China. When considering the data of Yoshino and coworkers, the transition zone conductivity models beneath southeast China are in more agreement with a dry laboratory model. Although the results are different when using different laboratory data, the estimated water content in the mantle transition zone beneath southeast China is less than 0.01 wt% irrespective of which laboratory data is used, suggesting a dry mantle transition zone beneath southeast China.

#### 4.7. Discussion and Suggestions

Using the multi-resolution finite element modeling tool, we have systematically investigated the local ocean effects for several unused coastal observatories in southeast China, which were excluded from previous global EM studies (Yuan et al., 2020). Although different mesh resolutions are needed for different observatories, our model studies indicated that at least for coastal observatories in China, a mesh with 1° angular resolution is adequate for accurately modeling the local ocean effects.

To obtain a reliable local 1D conductivity structure, accurate consideration of the surface ocean effects is needed. In the conventional ocean effect correction method, a prior 1D mantle structure is assumed, which may affect the final inverse model. The rigorous approach to account for the ocean effects is to perform the so-called quasi-1D inversion (Munch et al., 2018), in which a 3D forward operator is invoked during 1D inversion. However, this approach is computationally demanding. Therefore, we have adopted an alternative approach by making the ocean effect correction and 1D inversion iterated (Shimizu, Koyama, et al., 2010; Utada et al., 2003). Our results showed that this approach can converge to the final inverse solutions after 2 ~ 3 iterations. Therefore, we suggest using the iterative correction and inversion approach first, if it can not converge or a large data misfit is obtained, we then apply the rigorous 3D forward operator approach.

Although several global and semi-global 3D conductivity models have revealed low conductivity anomalies in southeast China (Fukao et al., 2004; Kelbert et al., 2009; Li et al., 2020; Semenov & Kuvshinov, 2012; Shimizu, Utada, et al., 2010; Sun et al., 2015), both the lateral and the radial resolutions are relatively low. We, therefore, analyzed several unused coastal observatory data by carefully accounting for the local ocean effects and obtained three new 1D conductivity models. Our high-resolution 1D models further confirmed the low conductivity structures. By comparing with the latest laboratory conductivity models, our models suggest a

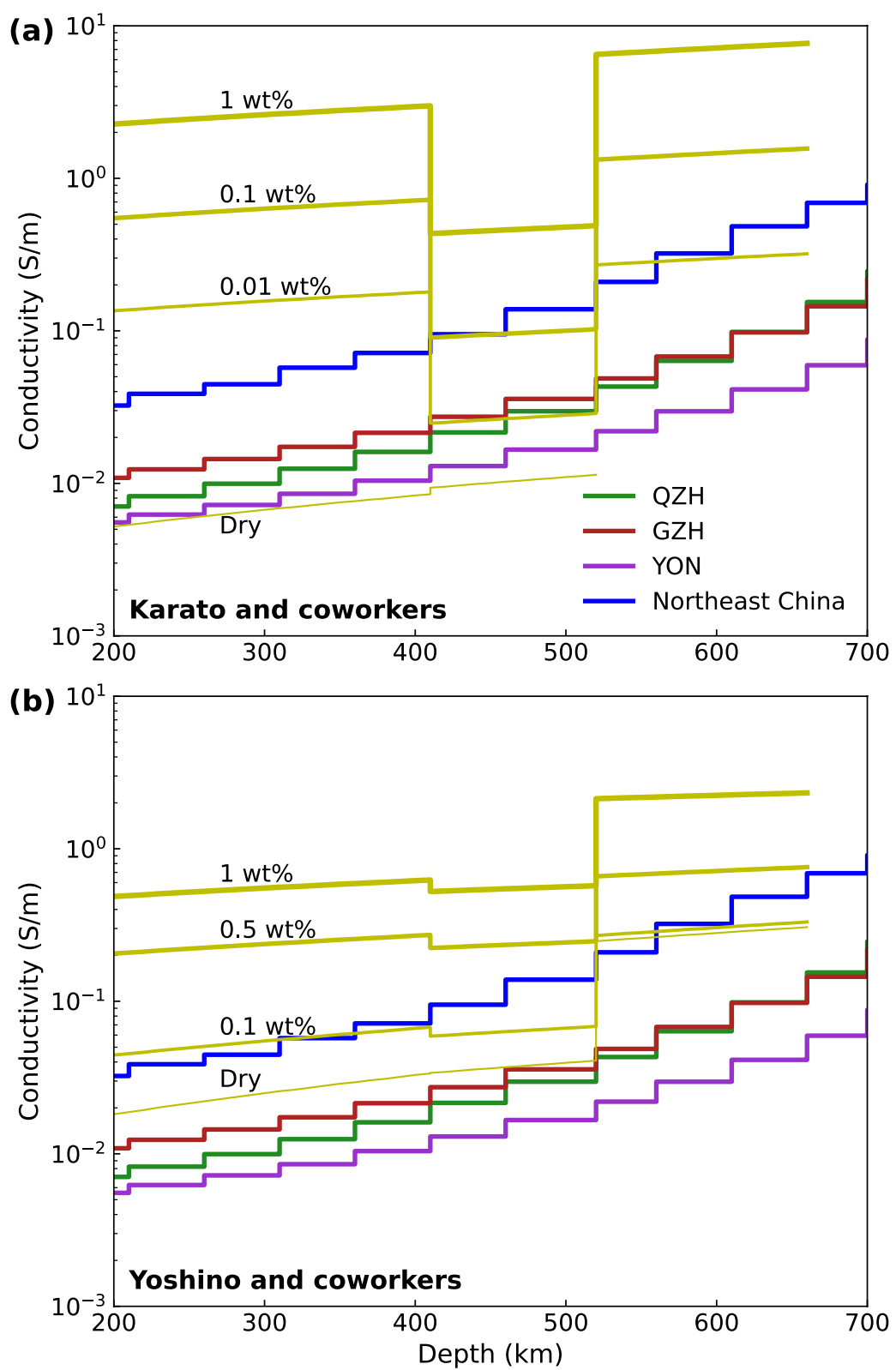


Figure 18.

water-poor mantle transition zone beneath southeast China (less than 0.01 wt%) irrespective of which laboratory data (Karato, 2011; Yoshino, 2010) is used. Note that in constructing the laboratory conductivity models in the transition zone, only the most abundant minerals (wadsleyite and ringwoodite) were considered. One may argue that other mineral such as garnet may affect our water content estimation. However, as discussed in the study by Matsuno et al. (2017), the second abundant transition zone mineral garnet can hardly affect the estimation of water content because the water solubility of garnet is much smaller than that of wadsleyite. Recently, a high-resolution seismic tomography model was derived beneath east-central China (Z. Huang et al., 2021), which revealed widespread low-velocity anomalies in the mantle transition zone beneath southeast China. These low-velocity anomalies suggest a higher temperature structure. Therefore, lower water content may be needed to explain the low conductivity, the mantle transition zone beneath southeast China is likely to dry.

This study concentrates on the transition zone structures, therefore, only considering the geomagnetic variations due to magnetospheric ring current is reasonable since they can provide good resolution in and below the mantle transition zone (Kelbert et al., 2008, 2009). In spite of this, including the geomagnetic Sq variations and magnetotelluric impedance data, which have better resolution in the upper mantle and crust, is desirable. Therefore, one of our future works is to perform a more comprehensive 1D study using geomagnetic observatory and magnetotelluric data over continental China. In the meanwhile, a natural step is to develop a new 3D multi-resolution inversion method based on this FE solver to jointly invert multi-source EM data measured by ground-based observatories and geomagnetic satellites to obtain more reliable structures. These considerations are beyond the scope of this work but will be discussed in our future study.

## 5. Conclusions

In this study, we have developed a new multi-source, multi-resolution global EM forward modeling solver using tetrahedral finite elements. This solver can deal with both magnetospheric and ionospheric current sources. Numerical results validated the correctness of our new modeling tool. Besides, the results showed that for one period and for problems with several million to hundred millions of unknowns, our solver can obtain accurate solutions in a few minutes on a cluster using up to 128 MPI processes. Further efficiency can be obtained thanks to its fully parallel implementation.

Using this multi-resolution modeling tool to accurately account for the near-surface ocean induction effects at several unused Chinese coastal geomagnetic observatories, we obtained three layered conductivity models beneath southeast China and one conductivity model beneath northeast China. We found that the conductivity value beneath southeast China is more than half an order of magnitude smaller than that beneath northeast China. We also compared our inverse conductivity models with the latest laboratory-measured conductivity data and seismic velocity models and found a dry mantle transition zone beneath southeast China with water content less than 0.01 wt%.

In conclusion, our forward modeling approach satisfies the new requirements of interpreting nowadays global EM induction data, such as the capabilities of computing multi-source EM responses, multi-resolution modeling of the near-surface conductive heterogeneities, and offering accurate EM responses on arbitrary 3D conductivity distributions, fast dealing with a large number of unknowns. Therefore, we believe that we have presented alternative and competitive finite-element solutions to global EM induction problems. It can be used as a reference forward solution as well as the core forward engine for global EM inversion.

## Data Availability Statement

The forward solutions, global near-surface conductance map, observed C-responses, inverse conductivity models, and the corresponding plotting scripts can be accessed at Zenodo (<https://doi.org/10.5281/zenodo.6720530>). For constructing the global conductance map presented in Figure 10, the CRUST1.0 model (Laske et al., 2013) can be

**Figure 18.** Comparison of our inverse conductivity models (QZH, GZH, YON, Northeast China) with laboratory conductivity models for various water content of (a) Karato and coworkers and (b) Yoshino and coworkers. The laboratory conductivity models of Karato and coworkers were constructed from the data of Wang et al. (2006) for olivine, Dai and Karato (2009) for wadsleyite, X. Huang et al. (2005) for ringwoodite. While those of Yoshino and coworkers were constructed from the data of Yoshino et al. (2009) for olivine, Yoshino and Katsura (2012) for wadsleyite, Yoshino et al. (2008) for ringwoodite. For the computation of these laboratory conductivity models, the latest adiabatic temperature profile (Katsura, 2022) was assumed.

accessed at <https://igppweb.ucsd.edu/~gabi/crust1.html>, the global 5 arc min sediment model GlobSed (Straume et al., 2019) can be accessed at <https://ngdc.noaa.gov/mgg/sedthick/>, the 3D ocean conductivity model (Tyler et al., 2017) can be accessed at <https://www.ngdc.noaa.gov/OC5/woa13/>. For constructing the laboratory conductivity model presented in Figure 18, the adiabatic temperature profile (Katsura, 2022) can be accessed at <https://zenodo.org/record/5903286>. The meshing tool used to generate multi-resolution tetrahedral grids, the inversion code used to generate the conductivity models, and the Matlab scripts used to construct the laboratory conductivity-depth profiles can be accessed at Zenodo (<https://doi.org/10.5281/zenodo.6720565>).

## Acknowledgments

This work was financially supported by the National Natural Science Foundation of China (41922027, 41830107, 4214200052), Innovation-Driven Project of Central South University (2020CX0012), Macau Foundation, and Macau Science and Technology Development Fund (0001/2019/A1), the Pre-research Project on Civil Aerospace Technologies funded by China National Space Administration (D020303), the Hunan Provincial Innovation Foundation for Postgraduate (CX20210277), and the Fundamental Research Funds for the Central Universities of Central South University (2021zzts0259). This work was supported in part by the High-Performance Computing Center of Central South University. The authors thank the Geomagnetic Network Center of China for providing the geomagnetic data. We thank Yi Zhang for kindly providing the spherical triangular tessellation tool for surface triangular mesh generation. We would like to thank Zdeněk Martinec for kindly offering analytic solutions for comparison and Hisayoshi Shimizu for kindly offering the 1D conductivity profiles beneath the north Pacific. Chaojian Chen is highly appreciated for helpful discussion and for providing the integral equation solutions of X3DG code (Kuvshinov, 2008) for comparison. The constructive comments by the associate editor Qinghua Huang, Colin Farquharson, and an anonymous reviewer have greatly helped to improve the manuscript.

## References

- Anderson, R., Andrej, J., Barker, A., Bramwell, J., Camier, J.-S., Cerveny, J., et al. (2021). Mfem: A modular finite element methods library. *Computers & Mathematics with Applications*, 81, 42–74. <https://doi.org/10.1016/j.camwa.2020.06.009>
- Arnold, D., Mukherjee, A., & Pouly, L. (2000). Locally adapted tetrahedral meshes using bisection. *SIAM Journal on Scientific Computing*, 22(2), 431–448. <https://doi.org/10.1137/s1064827597323373>
- Baker, A. H., Falgout, R. D., Kolev, T. V., & Yang, U. M. (2012). Scaling hypre's multigrid solvers to 100,000 cores. In *High-performance scientific computing* (pp. 261–279). Springer London. [https://doi.org/10.1007/978-1-4471-2437-5\\_13](https://doi.org/10.1007/978-1-4471-2437-5_13)
- Banks, R. J. (1969). Geomagnetic variations and the electrical conductivity of the upper mantle. *Geophysical Journal International*, 17(5), 457–487. <https://doi.org/10.1111/j.1365-246x.1969.tb00252.x>
- Brenner, S. C., & Scott, L. R. (2008). The mathematical theory of finite element methods. Springer. <https://doi.org/10.1007/978-0-387-75934-0>
- Castillo-Reyes, O., de la Puente, J., García-Castillo, L. E., & Cela, J. M. (2019). Parallel 3-D marine controlled-source electromagnetic modelling using high-order tetrahedral nédélec elements. *Geophysical Journal International*, 219(1), 39–65. <https://doi.org/10.1093/gji/ggz285>
- Chave, A. D., & Thomson, D. J. (1989). Some comments on magnetotelluric response function estimation. *Journal of Geophysical Research*, 94(B10), 14215–14225. <https://doi.org/10.1029/jb094b10p14215>
- Chen, C., Kruglyakov, M., & Kuvshinov, A. (2020). A new method for accurate and efficient modeling of the local ocean induction effects: Application to long-period responses from island geomagnetic observatories. *Geophysical Research Letters*, 47(8). <https://doi.org/10.1029/2019gl086351>
- Chen, J., Chen, Z., Cui, T., & Zhang, L.-B. (2010). An adaptive finite element method for the eddy current model with circuit/field couplings. *SIAM Journal on Scientific Computing*, 32(2), 1020–1042. <https://doi.org/10.1137/080713112>
- Constable, S. C., Parker, R. L., & Constable, C. G. (1987). Occam's inversion: A practical algorithm for generating smooth models from electromagnetic sounding data. *Geophysics*, 52(3), 289–300. <https://doi.org/10.1190/1.1442303>
- Dai, L., & Karato, S.-i. (2009). Electrical conductivity of wadsleyite at high temperatures and high pressures. *Earth and Planetary Science Letters*, 287(1–2), 277–283. <https://doi.org/10.1016/j.epsl.2009.08.012>
- Deschamps, F., & Khan, A. (2016). Electrical conductivity as a constraint on lower mantle thermo-chemical structure. *Earth and Planetary Science Letters*, 450, 108–119. <https://doi.org/10.1016/j.epsl.2016.06.027>
- Egbert, G. D., Alken, P., Maute, A., & Zhang, H. (2021). Modelling diurnal variation magnetic fields due to ionospheric currents. *Geophysical Journal International*, 225(2), 1086–1109. <https://doi.org/10.1093/gji/gja533>
- Everett, M. E., Constable, S., & Constable, C. G. (2003). Effects of near-surface conductance on global satellite induction responses. *Geophysical Journal International*, 153(1), 277–286. <https://doi.org/10.1046/j.1365-246x.2003.01906.x>
- Everett, M. E., & Schultz, A. (1996). Geomagnetic induction in a heterogenous sphere: Azimuthally symmetric test computations and the response of an undulating 660-km discontinuity. *Journal of Geophysical Research*, 101(B2), 2765–2783. <https://doi.org/10.1029/95jb03541>
- Fujii, I., & Schultz, A. (2002). The 3D electromagnetic response of the Earth to ring current and auroral oval excitation. *Geophysical Journal International*, 151(3), 689–709. <https://doi.org/10.1046/j.1365-246x.2002.01775.x>
- Fukao, Y., Koyama, T., Obayashi, M., & Utada, H. (2004). Trans-Pacific temperature field in the mantle transition region derived from seismic and electromagnetic tomography. *Earth and Planetary Science Letters*, 217(3–4), 425–434. [https://doi.org/10.1016/s0012-821x\(03\)00610-1](https://doi.org/10.1016/s0012-821x(03)00610-1)
- Fukao, Y., Obayashi, M., & Nakakuki, T. (2009). Stagnant slab: A review. *Annual Review of Earth and Planetary Sciences*, 37(1), 19–46. <https://doi.org/10.1146/annurev.earth.36.031207.124224>
- Geuzaine, C., & Remacle, J.-F. (2009). Gmsh: A 3-D finite element mesh generator with built-in pre- and post-processing facilities. *International Journal for Numerical Methods in Engineering*, 79(11), 1309–1331. <https://doi.org/10.1002/nme.2579>
- Grayver, A. V., & Kolev, T. V. (2015). Large-scale 3D geoelectromagnetic modeling using parallel adaptive high-order finite element method. *Geophysics*, 80(6), E277–E291. <https://doi.org/10.1190/geo2015-0013.1>
- Grayver, A. V., Kuvshinov, A., & Werthmüller, D. (2021). Time-domain modeling of three-dimensional Earth's and planetary electromagnetic induction effect in ground and satellite observations. *Journal of Geophysical Research: Space Physics*, 126(3). <https://doi.org/10.1029/2020ja028672>
- Grayver, A. V., Munch, F. D., Kuvshinov, A. V., Khan, A., Sabaka, T. J., & Tøffner-Clausen, L. (2017). Joint inversion of satellite-detected tidal and magnetospheric signals constrains electrical conductivity and water content of the upper mantle and transition zone. *Geophysical Research Letters*, 44(12), 6074–6081. <https://doi.org/10.1002/2017gl073446>
- Grayver, A. V., van Driel, M., & Kuvshinov, A. V. (2019). Three-dimensional magnetotelluric modelling in spherical Earth. *Geophysical Journal International*, 217(1), 532–557. <https://doi.org/10.1093/gji/ggz030>
- Guzavina, M., Grayver, A., & Kuvshinov, A. (2019). Probing upper mantle electrical conductivity with daily magnetic variations using global-to-local transfer functions. *Geophysical Journal International*, 219(3), 2125–2147. <https://doi.org/10.1093/gji/ggz412>
- Hamano, Y. (2002). A new time-domain approach for the electromagnetic induction problem in a three-dimensional heterogeneous Earth. *Geophysical Journal International*, 150(3), 753–769. <https://doi.org/10.1046/j.1365-246x.2002.01746.x>
- Hansen, P. C. (1992). Analysis of discrete ill-posed problems by means of the L-curve. *SIAM Review*, 34(4), 561–580. <https://doi.org/10.1137/1034115>
- Huang, X., Xu, Y., & ichiro Karato, S. (2005). Water content in the transition zone from electrical conductivity of wadsleyite and ringwoodite. *Nature*, 434(7034), 746–749. <https://doi.org/10.1038/nature03426>
- Huang, Z., Gou, T., & Wang, L. (2021). P and S wave tomography of east-central China: Insight into past and present mantle dynamics. *Tectonophysics*, 809, 228859. <https://doi.org/10.1016/j.tecto.2021.228859>

- Ichiki, M., Uyeshima, M., Utada, H., Guoze, Z., Ji, T., & Mingzhi, M. (2001). Upper mantle conductivity structure of the back-arc region beneath northeastern China. *Geophysical Research Letters*, 28(19), 3773–3776. <https://doi.org/10.1029/2001gl012983>
- Jin, J.-M. (2014). *The finite element method in electromagnetics* (3rd ed.). Wiley-IEEE Press.
- Karato, S.-i. (2011). Water distribution across the mantle transition zone and its implications for global material circulation. *Earth and Planetary Science Letters*, 301(3–4), 413–423. <https://doi.org/10.1016/j.epsl.2010.11.038>
- Karypis, G., & Kumar, V. (1998). A fast and high quality multilevel scheme for partitioning irregular graphs. *SIAM Journal on Scientific Computing*, 20(1), 359–392. <https://doi.org/10.1137/s1064827592287997>
- Katsura, T. (2022). A revised adiabatic temperature profile for the mantle. *Journal of Geophysical Research: Solid Earth*, 127(2). <https://doi.org/10.1029/2021jb023562>
- Kelbert, A., Egbert, G. D., & Schultz, A. (2008). Non-linear conjugate gradient inversion for global EM induction: Resolution studies. *Geophysical Journal International*, 173(2), 365–381. <https://doi.org/10.1111/j.1365-246x.2008.03717.x>
- Kelbert, A., Kuvshinov, A., Velimsky, J., Koyama, T., Ribaudo, J., Sun, J., et al. (2014). Global 3-D electromagnetic forward modelling: A benchmark study. *Geophysical Journal International*, 197(2), 785–814. <https://doi.org/10.1093/gji/ggu028>
- Kelbert, A., Schultz, A., & Egbert, G. (2009). Global electromagnetic induction constraints on transition-zone water content variations. *Nature*, 460(7258), 1003–1006. <https://doi.org/10.1038/nature08257>
- Khan, A., & Shankland, T. (2012). A geophysical perspective on mantle water content and melting: Inverting electromagnetic sounding data using laboratory-based electrical conductivity profiles. *Earth and Planetary Science Letters*, 317–318, 27–43. <https://doi.org/10.1016/j.epsl.2011.11.031>
- Koch, S., & Kuvshinov, A. (2015). 3-D EM inversion of ground based geomagnetic Sq data. Results from the analysis of Australian array (AWAGS) data. *Geophysical Journal International*, 200(3), 1284–1296. <https://doi.org/10.1093/gji/ggu474>
- Kolev, T. V., & Vassilevski, P. S. (2009). Parallel auxiliary space AMG for H(Curl) problems. *Journal of Computational Mathematics*, 27(5), 604–623. <https://doi.org/10.4208/jcm.2009.27.5.013>
- Koyama, T., Khan, A., & Kuvshinov, A. (2014). Three-dimensional electrical conductivity structure beneath Australia from inversion of geomagnetic observatory data: Evidence for lateral variations in transition-zone temperature, water content and melt. *Geophysical Journal International*, 196(3), 1330–1350. <https://doi.org/10.1093/gji/ggt455>
- Kushiro, I., Syono, Y., & ichi Akimoto, S. (1968). Melting of a peridotite nodule at high pressures and high water pressures. *Journal of Geophysical Research*, 73(18), 6023–6029. <https://doi.org/10.1029/jb073i018p06023>
- Kuvshinov, A. (2008). 3-D global induction in the oceans and solid Earth: Recent progress in modeling magnetic and electric fields from sources of magnetospheric, ionospheric and oceanic origin. *Surveys in Geophysics*, 29(2), 139–186. <https://doi.org/10.1007/s10712-008-9045-z>
- Kuvshinov, A. (2012). Deep electromagnetic studies from land, sea, and space: Progress status in the past 10 years. *Surveys in Geophysics*, 33(1), 169–209. <https://doi.org/10.1007/s10712-011-9118-2>
- Kuvshinov, A., Grayver, A., Tøffner-Clausen, L., & Olsen, N. (2021). Probing 3-D electrical conductivity of the mantle using 6 years of Swarm, CryoSat-2 and observatory magnetic data and exploiting matrix Q-responses approach. *Earth Planets and Space*, 73(1), 63. <https://doi.org/10.1186/s40623-020-01341-9>
- Kuvshinov, A., & Olsen, N. (2006). A global model of mantle conductivity derived from 5 years of CHAMP, Ørsted, and SAC-C magnetic data. *Geophysical Research Letters*, 33(18). <https://doi.org/10.1029/2006gl027083>
- Kuvshinov, A., Olsen, N., Avdeev, D. B., & Pankratov, O. V. (2002). Electromagnetic induction in the oceans and the anomalous behaviour of coastal C-responses for periods up to 20 days. *Geophysical Research Letters*, 29(12). <https://doi.org/10.1029/2001gl014409>
- Kuvshinov, A., & Semenov, A. (2012). Global 3-D imaging of mantle electrical conductivity based on inversion of observatory C-responses-I. An approach and its verification. *Geophysical Journal International*, 189(3), 1335–1352. <https://doi.org/10.1111/j.1365-246x.2011.05349.x>
- Kuvshinov, A., Utada, H., Avdeev, D., & Koyama, T. (2005). 3-D modelling and analysis of Dst C-responses in the North Pacific Ocean region, revisited. *Geophysical Journal International*, 160(2), 505–526. <https://doi.org/10.1111/j.1365-246x.2005.02477.x>
- Laske, G., Masters, G., Z., M., & Pasquano, M. (2013). Update on CRUST1.0 - A 1-degree global model of Earth's crust. *Geophys. Res. Abstracts*, 15, 2658. Abstract EGU2013.
- Li, S., Weng, A., Zhang, Y., Schultz, A., Li, Y., Tang, Y., et al. (2020). Evidence of Bermuda hot and wet upwelling from novel three-dimensional global mantle electrical conductivity image. *Geochemistry, Geophysics, Geosystems*, 21(6). <https://doi.org/10.1029/2020gc009016>
- Martinec, Z. (1998). Geomagnetic induction in multiple eccentrically nested spheres. *Geophysical Journal International*, 132(1), 96–110. <https://doi.org/10.1046/j.1365-246x.1998.00392.x>
- Martinec, Z. (1999). Spectral-finite element approach to three-dimensional electromagnetic induction in a spherical Earth. *Geophysical Journal International*, 136(1), 229–250. <https://doi.org/10.1046/j.1365-246x.1999.00713.x>
- Matsuno, T., Suetegu, D., Baba, K., Tada, N., Shimizu, H., Shiobara, H., et al. (2017). Mantle transition zone beneath a normal seafloor in the northwestern Pacific: Electrical conductivity, seismic thickness, and water content. *Earth and Planetary Science Letters*, 462, 189–198. <https://doi.org/10.1016/j.epsl.2016.12.045>
- Mei, S., & Kohlstedt, D. L. (2000). Influence of water on plastic deformation of olivine aggregates: 1. Diffusion creep regime. *Journal of Geophysical Research*, 105(B9), 21457–21469. <https://doi.org/10.1029/2000jb900179>
- Munch, F. D., Grayver, A. V., Kuvshinov, A., & Khan, A. (2018). Stochastic inversion of geomagnetic observatory data including rigorous treatment of the ocean induction effect with implications for transition zone water content and thermal structure. *Journal of Geophysical Research: Solid Earth*, 123(1), 31–51. <https://doi.org/10.1002/2017jb014691>
- Nédélec, J. C. (1980). Mixed finite elements in R3. *Numerische Mathematik*, 35(3), 315–341. <https://doi.org/10.1007/bf01396415>
- Nocedal, J., & Wright, S. J. (2006). *Numerical optimization*. Springer.
- Oden, J., & Prudhomme, S. (2001). Goal-oriented error estimation and adaptivity for the finite element method. *Computers & Mathematics with Applications*, 41(5–6), 735–756. [https://doi.org/10.1016/s0898-1221\(00\)00317-5](https://doi.org/10.1016/s0898-1221(00)00317-5)
- Püthe, C., Kuvshinov, A., Khan, A., & Olsen, N. (2015). A new model of Earth's radial conductivity structure derived from over 10 yr of satellite and observatory magnetic data. *Geophysical Journal International*, 203(3), 1864–1872. <https://doi.org/10.1093/gji/ggv407>
- Qiu, C., Yin, C., Liu, Y., Ren, X., Chen, H., & Yan, T. (2021). Solution of large-scale 3D controlled-source electromagnetic modeling problem using efficient iterative solvers. *Geophysics*, 86(4), E283–E296. <https://doi.org/10.1190/geo2020-0461.1>
- Ren, Z., Kalscheuer, T., Greenhalgh, S., & Maurer, H. (2013). A goal-oriented adaptive finite-element approach for plane wave 3-D electromagnetic modelling. *Geophysical Journal International*, 194(2), 700–718. <https://doi.org/10.1093/gji/ggt154>
- Ribaudo, J. T., Constable, C. G., & Parker, R. L. (2012). Scripted finite element tools for global electromagnetic induction studies. *Geophysical Journal International*, 188(2), 435–446. <https://doi.org/10.1093/gji/gji05255>
- Romanowicz, B. (2003). Global mantle tomography: Progress status in the past 10 years. *Annual Review of Earth and Planetary Sciences*, 31(1), 303–328. <https://doi.org/10.1146/annurev.earth.31.091602.113555>

- Saad, Y. (2003). Iterative methods for sparse linear systems. *Society for Industrial and Applied Mathematics*. <https://doi.org/10.1137/1.9780898718003>
- Schmucker, U. (1985). Spherical harmonics in geomagnetism. In *Landolt-börnstein - group v geophysics* (pp. 68–71). Springer-Verlag. [https://doi.org/10.1007/10201925\\_20](https://doi.org/10.1007/10201925_20)
- Schmucker, U. (1999). A spherical harmonic analysis of solar daily variations in the years 1964–1965: Response estimates and source fields for global induction-i. Methods. *Geophysical Journal International*, 136(2), 439–454. <https://doi.org/10.1046/j.1365-246x.1999.00742.x>
- Semenov, A., & Kuvшинов, A. (2012). Global 3-D imaging of mantle conductivity based on inversion of observatory C-responses-II. Data analysis and results. *Geophysical Journal International*, 191(3), 965–992. <https://doi.org/10.1111/j.1365-246x.2012.05665.x>
- Shimizu, H., Koyama, T., Baba, K., & Utada, H. (2010). Revised 1-D mantle electrical conductivity structure beneath the north Pacific. *Geophysical Journal International*, 180(3), 1030–1048. <https://doi.org/10.1111/j.1365-246x.2009.04466.x>
- Shimizu, H., Utada, H., Baba, K., Koyama, T., Obayashi, M., & Fukao, Y. (2010). Three-dimensional imaging of electrical conductivity in the mantle transition zone beneath the North Pacific Ocean by a semi-global induction study. *Physics of the Earth and Planetary Interiors*, 183(1–2), 252–269. <https://doi.org/10.1016/j.pepi.2010.01.010>
- Straume, E. O., Gaina, C., Medvedev, S., Hochmuth, K., Gohl, K., Whittaker, J. M., et al. (2019). GlobSed: Updated total sediment thickness in the world's oceans. *Geochemistry, Geophysics, Geosystems*, 20(4), 1756–1772. <https://doi.org/10.1029/2018gc008115>
- Sun, J., & Egbert, G. D. (2012). A thin-sheet model for global electromagnetic induction. *Geophysical Journal International*, 189(1), 343–356. <https://doi.org/10.1111/j.1365-246x.2012.05383.x>
- Sun, J., Kelbert, A., & Egbert, G. D. (2015). Ionospheric current source modeling and global geomagnetic induction using ground geomagnetic observatory data. *Journal of Geophysical Research: Solid Earth*, 120(10), 6771–6796. <https://doi.org/10.1002/2015jb012063>
- Tarits, P., & Mandéa, M. (2010). The heterogeneous electrical conductivity structure of the lower mantle. *Physics of the Earth and Planetary Interiors*, 183(1–2), 115–125. <https://doi.org/10.1016/j.pepi.2010.08.002>
- Tyler, R. H., Boyer, T. P., Minami, T., Zweng, M. M., & Reagan, J. R. (2017). Electrical conductivity of the global ocean. *Earth Planets and Space*, 69(1). <https://doi.org/10.1186/s40623-017-0739-7>
- Utada, H., Koyama, T., Obayashi, M., & Fukao, Y. (2009). A joint interpretation of electromagnetic and seismic tomography models suggests the mantle transition zone below Europe is dry. *Earth and Planetary Science Letters*, 281(3–4), 249–257. <https://doi.org/10.1016/j.epsl.2009.02.027>
- Utada, H., Koyama, T., Shimizu, H., & Chave, A. D. (2003). A semi-global reference model for electrical conductivity in the mid-mantle beneath the north Pacific region. *Geophysical Research Letters*, 30(4). <https://doi.org/10.1029/2002gl016092>
- Ueyshima, M., & Schultz, A. (2000). Geoelectromagnetic induction in a heterogeneous sphere: new three-dimensional forward solver using a conservative staggered-grid finite difference method. *Geophysical Journal International*, 140(3), 636–650. <https://doi.org/10.1046/j.1365-246x.2000.00051.x>
- Velímský, J., & Finlay, C. C. (2011). Effect of a metallic core on transient geomagnetic induction. *Geochemistry, Geophysics, Geosystems*, 12(5). <https://doi.org/10.1029/2011gc003557>
- Velímský, J., & Knopp, O. (2021). Lateral variations of electrical conductivity in the lower mantle constrained by Swarm and CryoSat-2 missions. *Earth Planets and Space*, 73(1). <https://doi.org/10.1186/s40623-020-01334-8>
- Velímský, J., & Martinec, Z. (2005). Time-domain, spherical harmonic-finite element approach to transient three-dimensional geomagnetic induction in a spherical heterogeneous Earth. *Geophysical Journal International*, 161(1), 81–101. <https://doi.org/10.1111/j.1365-246x.2005.02546.x>
- Wang, D., Mookherjee, M., Xu, Y., & Ichiro Karato, S. (2006). The effect of water on the electrical conductivity of olivine. *Nature*, 443(7114), 977–980. <https://doi.org/10.1038/nature05256>
- Wei, S. S., & Chen, Y. J. (2016). Seismic evidence of the Hainan mantle plume by receiver function analysis in southern China. *Geophysical Research Letters*, 43(17), 8978–8985. <https://doi.org/10.1002/2016gl069513>
- Weidelt, P. (1972). The inverse problem of geomagnetic induction. *Journal of Geophysics*, 38, 257–289. <https://doi.org/10.1093/gji/35.1.379>
- Weiss, C. J. (2010). Triangulated finite difference methods for global-scale electromagnetic induction simulations of whole mantle electrical heterogeneity. *Geochemistry, Geophysics, Geosystems*, 11. <https://doi.org/10.1029/2010gc003283>
- Weiss, C. J. (2014). An overset grid method for global geomagnetic induction. *Geophysical Journal International*, 198(1), 8–24. <https://doi.org/10.1093/gji/ggu108>
- Weiss, C. J., & Everett, M. E. (1998). Geomagnetic induction in a heterogeneous sphere: Fully three-dimensional test computations and the response of a realistic distribution of oceans and continents. *Geophysical Journal International*, 135(2), 650–662. <https://doi.org/10.1046/j.1365-246x.1998.00670.x>
- Yoshimura, R., & Oshiman, N. (2002). Edge-based finite element approach to the simulation of geoelectromagnetic induction in a 3-D sphere. *Geophysical Research Letters*, 29(3). <https://doi.org/10.1029/2001gl014121>
- Yoshino, T. (2010). Laboratory electrical conductivity measurement of mantle minerals. *Surveys in Geophysics*, 31(2), 163–206. <https://doi.org/10.1007/s10712-009-9084-0>
- Yoshino, T., & Katsura, T. (2012). Re-evaluation of electrical conductivity of anhydrous and hydrous wadsleyite. *Earth and Planetary Science Letters*, 337–338, 56–67. <https://doi.org/10.1016/j.epsl.2012.05.023>
- Yoshino, T., Manthilake, G., Matsuzaki, T., & Katsura, T. (2008). Dry mantle transition zone inferred from the conductivity of wadsleyite and ringwoodite. *Nature*, 451(7176), 326–329. <https://doi.org/10.1038/nature06427>
- Yoshino, T., Matsuzaki, T., Shatskiy, A., & Katsura, T. (2009). The effect of water on the electrical conductivity of olivine aggregates and its implications for the electrical structure of the upper mantle. *Earth and Planetary Science Letters*, 288(1–2), 291–300. <https://doi.org/10.1016/j.epsl.2009.09.032>
- Yuan, Y., Ueyshima, M., Huang, Q., Tang, J., Li, Q., & Teng, Y. (2020). Continental-scale deep electrical resistivity structure beneath China. *Tectonophysics*, 790, 228559. <https://doi.org/10.1016/j.tecto.2020.228559>
- Zhang, H., Egbert, G. D., Chave, A. D., Huang, Q., Kelbert, A., & Erofeeva, S. Y. (2019). Constraints on the resistivity of the oceanic lithosphere and asthenosphere from seafloor ocean tidal electromagnetic measurements. *Geophysical Journal International*, 219(1), 464–478. <https://doi.org/10.1093/gji/ggj278>
- Zhang, Y., Mooney, W. D., & Chen, C. (2018). Forward calculation of gravitational fields with variable resolution 3D density models using spherical triangular tessellation: Theory and Applications. *Geophysical Journal International*, 215(1), 363–374. <https://doi.org/10.1093/gji/ggy278>
- Zhang, Y., Weng, A., Li, S., Yang, Y., Tang, Y., & Liu, Y. (2020). Electrical conductivity in the mantle transition zone beneath Eastern China derived from L1-Norm C-responses. *Geophysical Journal International*, 221(2), 1110–1124. <https://doi.org/10.1093/gji/ggaa059>